

Understanding the correlation between electronic coupling and energetic stability of molecular crystal polymorphs: The instructive case of quinacridone.

Christian Winkler,¹ Andreas Jeindl,¹ Florian Mayer,¹ Oliver T. Hofmann,¹ Ralf Tonner,² and Egbert Zojer^{1,}*

¹ Institute of Solid State Physics, NAWI Graz, Graz University of Technology, Petersgasse 16, 8010 Graz, Austria

² Department of Chemistry, Philipps-Universität Marburg, Hans-Meerwein-Straße 4, 35032 Marburg, Germany

Organic semiconductors, charge-carrier mobilities, machine learning, tight-binding, transfer integrals, effective masses

A crucial factor determining charge transport in organic semiconductors is the electronic coupling between the molecular constituents, which is heavily influenced by the relative arrangement of the molecules. This renders quinacridone, with its multiple, structurally fundamentally different polymorphs and their diverse intermolecular interactions an ideal test case for analyzing the correlation between the electronic coupling in a specific configuration and the configuration's energetic stability. To provide an in-depth analysis of this correlation, starting from the α -polymorph of quinacridone, we also construct a coplanar model crystal. This allows us to systematically compare the displacement-dependence of the electronic coupling with that of the total energy. In this way, we identify the combination of Pauli repulsion and orbital rehybridization as the driving force steering the system towards a structure in which the electronic coupling is minimal (especially for the valence band and at small displacements). The general nature of these observations is supported by equivalent trends for an analogous pentacene model system. This underlines that the design of high-performance materials cannot rely on the "natural" assembly of the π -conjugated backbones of organic semiconductors into their most stable configurations. Rather, it must include the incorporation of functional groups that steer crystal packing towards more favorable structures, where aiming for short-axis displacements or realizing comparably large long-axis displacements appear as strategies worthwhile exploring.

1. INTRODUCTION

Organic semiconductors (OSC) are increasingly used as active elements in (opto)electronic and photonic devices.¹⁻¹¹ For most of these applications, the charge-carrier mobility, μ , of the employed materials is of paramount importance. Unfortunately, carrier mobilities in the majority of OSCs are orders of magnitude smaller than in their inorganic counterparts.¹² Improving that situation and achieving efficient charge transport is, thus, one of the key challenges for the further success of OSC-based devices. Computational modelling has the potential to significantly contribute to overcoming that challenge by explaining the experimentally observed trends and by helping to understand, whether specific intermolecular interactions exist that drive molecular crystals towards low-mobility configurations. Based on such insights, it should eventually be possible to design new systems with markedly improved properties.

In order to simulate charge-carrier mobilities, many models have been developed over the years, with the limiting cases represented by fully coherent band transport (for weak electron-phonon coupling and low temperatures) and incoherent hopping (for strong electron-phonon coupling at elevated temperatures).¹³⁻¹⁶ The popularity of the various models has varied over time and their suitability for a given system typically depends on the types of molecules, their arrangement, the temperature range of interest, and the degree of disorder present.¹³⁻¹⁶ Essential parameters in all models are the electronic couplings between neighboring molecules, which are typically correlated with the overlap of the associated wavefunctions and are often expressed via so-called transfer integrals, t . For hopping-based theories the carrier mobility, μ , is then proportional to t^2 , while it is proportional to t for band-transport based models at least within a simple tight-binding picture.^{13,16} For complex cases, elaborate tight-binding fits are advisable for determining the electronic coupling in the actual crystalline environment. They

also allow a straightforward calculation of the effective mass of the charge carriers in the entire Brillouin zone.¹⁷

Besides small inter-molecular electronic couplings, charge transport in organic crystals is also limited by factors like a particularly strong electron-phonon coupling^{13–16} and the associated dynamic^{18–23} as well as static disorder. The focus of the present study, however, is on the materials' electronic properties (considering the material's full 3D crystalline structure), in order to determine fundamental factors that limit the electronic coupling.

A key aspect in this context is the relative geometric arrangement of neighboring molecules, where displacements by fractions of an Å can easily change transfer integrals by orders of magnitude.^{13,24–31} In other words, the structure of an organic semiconductor crystal crucially determines quantities describing its electronic properties, like band widths, transfer integrals and effective masses. This raises the question, whether a similar correlation also exists in the opposite direction, i.e., whether the magnitude of the electronic coupling between neighboring molecules in a crystal in a systematic way defines its (equilibrium) structure. To address this question, in the following we will search for correlations between inter-molecular electronic couplings (i.e., transfer integrals) and the energetic stability of specific structural motifs. The primary goal of this is to understand, whether there are driving forces that steer OSC crystals into equilibrium packing configurations with reduced electronic couplings. The latter is suggested by the observation that the highest mobilities are often found for metastable, high-energy phases.^{32,33} In fact, based on molecular dimer simulations, Sutton et al. have already suggested a “clear correlation between the degrees of intermolecular electronic coupling and exchange repulsion”.³⁴ Additionally, we will explore, whether alternative driving forces not immediately related to inter-molecular wavefunction overlaps, such as electrostatic or van der Waals interactions, might help mitigating this dilemma.

As the primary model system for our study, we chose the hydrogen-bonded organic pigment quinacridone, which has been successfully used in several devices, suggesting an avenue towards biocompatible electronics.¹⁹⁻²¹ Considering the presence of polar heteroatomic groups and the prevalence of hydrogen bonds, it also promises particularly rich physics to be explored. Quinacridone exhibits three established, stable polymorphs (called α , β and γ)³⁵ with fundamentally different packing motifs. Still, in all polymorphs one observes π -stacking of neighboring molecules,³⁵ rather than the more common herringbone arrangement.^{36,37} This is insofar interesting, as a cofacial π -stacking of molecules in brickwork or slip-stacked architectures has been observed for many high-mobility materials.^{28,38-40} Consequently, in the following, we will focus on analyzing the electronic coupling in the π -stacking direction. In this direction the largest coupling for a given material can be achieved, provided that the molecules are suitably arranged.

On more technical grounds, in the past the magnitude and sign of transfer integrals in OSCs have typically been rationalized based on calculations on displaced π -stacked molecular dimers together with the symmetries and nodal structures of the relevant dimer orbitals.²⁴⁻²⁹ For quinacridone, such a π -stacked arrangement of molecules is consistent with the actual crystal structure. Consequently, starting from the α -polymorph and without breaking the inter-molecular H-bonds, one can construct a representative crystalline model system with molecules arranged in parallel planes. For the sake of comparison, we also analyze an analogous model crystal built from pentacene molecules, even though pentacene crystallizes in a herringbone pattern. Displacing the molecular planes in the model systems relative to each other allows deriving the dependence of the transfer integrals on the inter-molecular displacement in a realistic, crystalline environment. Importantly, in contrast to simulating dimers, these calculations also provide direct information on how the total energy of the 3D extended system

depends on the displacement. This then allows identifying possible correlations between the magnitude of the transfer integral(s) and the stability of a specific crystalline structure.

2. Computational Methodology

2.1 General approach

Computationally, transfer integrals are usually either derived from molecular dimer simulations^{13,24–28} or from band-structure calculations. Based on the results of the latter (relying on a simple tight-binding ansatz), transfer integrals can be directly obtained from band widths.^{26,41} Consequently, (within certain limitations)¹⁷ also band widths serve as a measure for the inter-molecular electronic coupling. A more advanced approach is fitting more elaborate analytic expressions derived from tight-binding models (see below) to the bands in the entire 1st Brillouin zone. The transfer integrals to all relevant neighbors can then be extracted from that fit.^{14,17} Compared to calculations on molecular dimers, this has the advantage that the crystalline environment of the molecules is accounted for and situations can be identified in which “super exchange”-like next-nearest neighbor couplings become relevant.^{17,42–45} Thus, before correlating electronic couplings and total energies, we will first explore, whether simulations based on molecular dimers and calculations employing periodic boundary conditions yield consistent trends. As far as the periodic simulations are concerned, we will also test, whether trends derived from band widths and from tight-binding parameters are consistent.

For the dimer simulations, we extracted dimer geometries from the relaxed crystal structures (see below). To calculate their electronic structure, we employed the FHI-aims code,⁴⁶ version 180424 in combination with the Perdew-Burke-Enzerhof (PBE)^{47,48} functional and the default “tight” settings for the numerical parameters and basis sets (a more detailed description of the

nature of the associated basis sets can be found in the Supporting Information). Transfer integrals were determined from orbital energies applying the “energy splitting in dimer” (ESD) technique.¹³ As an alternative strategy, we also employed the fragment orbital (FO) approach²⁵ using a recently developed post-processing tool interfaced with FHI-aims.⁴⁹ The sign of the transfer integrals was determined depending on whether the bonding (positive) or antibonding (negative) linear combination of the molecular orbitals was higher in energy. Due to the inversion symmetry of the dimers, the transfer integrals obtained with the ESD and FO approaches are essentially identical when employing the PBE functional (as is shown in the Supporting Information).

For the calculations relying on periodic boundary conditions, we used dispersion-corrected density-functional theory (DFT). Unless otherwise stated, we used VASP 5.4.4^{50–53} treating exchange and correlation via the PBE functional in combination with the Tkatchenko-Scheffler (TS) dispersion correction method⁵⁴ to account for long-range van der Waals interactions. The recommended PAW⁵⁵ potentials (details in the Supporting Information) together with a plane-wave cut-off energy of 700 eV were used for all calculations. In the self-consistent-field (SCF) procedure, the Brillouin zone was sampled using a 32 x 20 x 8 Γ -centered k-point grid for α -, a 25 x 36 x 9 grid for β -, a 8 x 32 x 8 grid for γ -quinacridone, and a 25 x 25 x 25 grid for the coplanar model system. This k-point grid is significantly overconverged for determining a reliable charge density. It has been chosen here, as a particularly tight sampling of the Brillouin zone is necessary for improving the quality of the tight-binding fits and for determining meaningful total band widths (see below). Bearing this in mind, for the test of the employed methodology (functional and van der Waals correction) and for energy decompositions, smaller k-point grids have been used. To describe the occupation of the electronic states, we used the Methfessel-Paxton⁵⁶ occupation scheme with a width of 0.1 eV. The geometries of the α -, β -, and γ -polymorphs of quinacridone were obtained using the experimental unit cells,³⁵ and

relaxing the atomic positions of the molecule(s) until the largest force component on the atoms was smaller than 0.01 eV/Å.

2.2 Testing the impact of the type of van der Waals correction and the employed functional

As far as the choice of the *a posteriori* van der Waals correction is concerned, in addition to the above-mentioned TS approach, we also tested the many-body dispersion (MBD) approach by Ambrosetti et al.⁵⁷ As will be shown below, the choice of the vdW correction has virtually no impact on the relative stability of the different polymorphs (section 3.1), but it changes the order of minima of the total energy, when calculating the coplanar model crystal as a function of inter-molecular displacements (section 3.2). Both methods applied in this test, TS as well as MBD, build on the converged charge density. For obtaining the results of the computationally much more expensive MBD approach, the same energy cutoff as in section 2.1 has been used in VASP and we employed the following k-point grids: α -quinacridone - 16 x 10 x 4; β -quinacridone, - 13 x 8 x 4; γ -quinacridone – 4 x 16 x 4, and coplanar model crystal – 12 x 12 x 12. These grids are somewhat smaller than the ones described in section 2.1, as the MBD calculations have neither been used for determining total band widths nor for fitting tight-binding functions (see above). For the α -, β -, and γ -polymorphs of quinacridone, we also performed geometry optimizations using the MBD approach.

To test the impact of the employed functional (especially evaluating the role of exact exchange), we also performed calculations using the hybrid functional HSE06.^{59,60} This yields equivalent results for the nature of the frontier bands; only the band widths obtained with HSE are somewhat larger, as will be discussed in the results and discussion section. The only

qualitative change upon employing HSE vs. PBE concerns the order of deeper-lying orbitals (see Supporting Information of Ref. 17), consistent with the results of Lüftner et al.⁶¹ As we are primarily concerned with the frontier bands and since swapping the orbital ordering does not affect the electron density, this has also no effect on the quantities discussed here. Thus, we can safely rely on the (computationally much less expensive) PBE calculations

On more technical grounds, the HSE calculations have been performed using FHI-aims for both, open and periodic boundary conditions. This choice is made here, as for hybrid calculations we are typically able to achieve convergence particularly efficiently in FHI-aims. Notably, for the chosen (well converged) settings, test calculations employing the PBE functional in FHI-aims and in VASP yield identical band structures. For the HSE calculations in FHI-aims, the same well-converged k-point grids as for the MBD tests have been used for α -quinacridone, β -quinacridone, and γ -quinacridone. For the tests on the coplanar model crystal, we reduced the grid to 6 x 6 x 6 due to memory limitations.

2.3 Building the coplanar model crystal

As a first step to create the model crystal with quinacridone molecules arranged in parallel planes, we constructed an orthorhombic unit cell and then placed a gas-phase optimized quinacridone molecule in this cell such that the long molecular axis was parallel to the unit cell vector \mathbf{a}_3 , the short axis parallel to \mathbf{a}_2 , and the stacking direction of the molecules parallel to \mathbf{a}_1 (see Figure 1). The length of \mathbf{a}_1 was set to 3.5 Å (the equilibrium distance of the quinacridone stripes in the α -polymorph).³⁵ The lengths of \mathbf{a}_2 and \mathbf{a}_3 were chosen such that the van der Waals surfaces of neighboring molecules touched. Next, the lengths of the unit cell vectors \mathbf{a}_2 and \mathbf{a}_3 and the molecular geometry were relaxed, where for technical reasons associated with the partially constrained relaxations we employed the FHI-aims⁴⁶ code (see Supporting Information). All geometry optimizations for the model crystal were performed combining the

PBE functional with the TS van der Waals correction. Compared to simply arranging quinacridone molecules in their gas-phase geometry, this has the advantage that geometric changes due to the formation of inter-molecular H-bonds (i.e., a more aromatic structure of the molecules) are accounted for. In a second step, the size of the unit cell in \mathbf{a}_1 direction was doubled to 7.0 Å, such that it contained two molecules in the stacking direction (c.f., Figure 1). This setup allows to easily shift consecutive quinacridone layers in an AB fashion, see Figure 1. In passing we note that employing this procedure has hardly any impact on the H-bonding network of quinacridone. As discussed in more detail in the Supporting Information, the H-bonding energies are reduced by less than 3% in the orthorhombic model system compared to the α -polymorph and the bonding distances are even somewhat smaller. Notably, the procedure sketched here yields a model system that is reasonably close to the α -polymorph of quinacridone, as exemplified by the observation that the lowest-energy structure of the model system is only ca. 0.3 eV per molecule higher in energy than the α -polymorph.

For constructing the pentacene model crystals, we adopted the same strategy with the only difference that for the geometry optimizations we had to set the length of the \mathbf{a}_1 vector to a value large enough to suppress inter-layer interactions (40 Å), as otherwise unrealistic geometric distortions occurred (for details see Supporting Information).

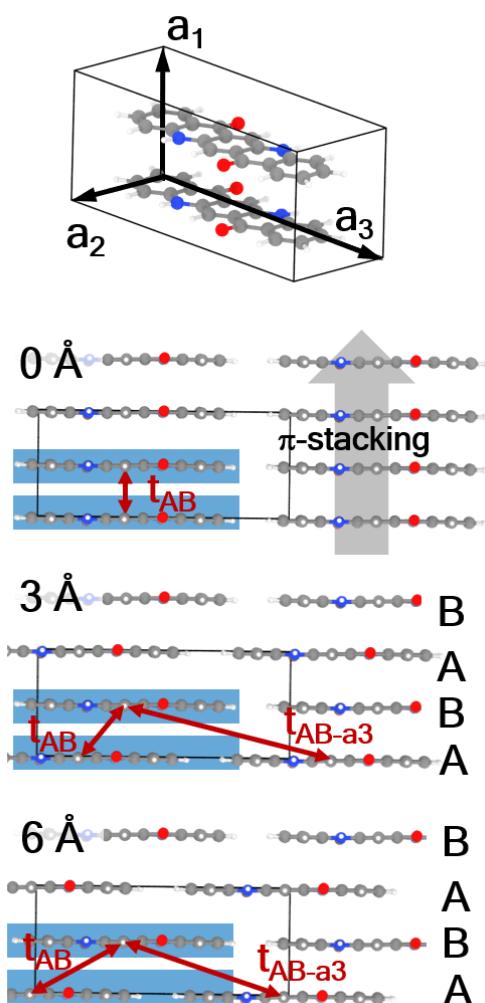


Figure 1. Unit cell of the coplanar model crystal derived from the α -phase of quinacridone.

The two most important transfer integrals for transport in π -stacking direction are sketched for 3 different displacements of the molecular layers.

2.4 Two-dimensional displacement maps, band widths and tight-binding fits

When calculating the energetics and band widths upon displacing neighboring quinacridone or pentacene planes in the model crystals, DFT calculations employing the comparably expensive settings from section 2.1 are performed for displacements along either the long or the short molecular axes. Doing such calculations on a sufficiently dense grid for simultaneous displacements along both axes would pose a sizable computational challenge. Thus, for such

2D displacement maps we, resorted to Gaussian process regression. There, the model vector consisted only of the x and y positions of the shifted layer and as kernel functions we chose linear combinations of Gaussian kernels equally distributed in the unit cell, which fulfill the periodicity constraints. To optimize the hyper parameters, the marginal log likelihood was maximized. Gaussian process regression allows to estimate a model error, which is visualized and discussed in the Supplementary Information. The model was first trained with the data calculated for displacements along the long and short molecular axes. Then 10 additional points were chosen at the coordinates of maximum model uncertainty. During this process all system symmetries (C_2 rotation around \mathbf{a}_1 for quinacridone and pentacene, mirroring along \mathbf{a}_2 and \mathbf{a}_3 for pentacene) were considered and exploited.

As far as band widths are concerned, the total band width, W , of α -quinacridone with only a single molecule in the unit cell is defined as the difference between the maximum and the minimum values of the energies of the highest occupied eigenstate for all considered \mathbf{k} -points. Band widths along specific \mathbf{k} -paths are determined in an analogous manner. In β -quinacridone, γ -quinacridone, and the coplanar model crystals, the situation is less straightforward, as these systems all contain two molecules per unit cell, which causes a backfolding of the bands. There, to obtain values consistent with the procedure for α -quinacridone, W was determined by subtracting the maximum energy amongst the highest occupied eigenstates in the entire 1st Brillouin zone from the minimum of the second highest occupied eigenstates. For \mathbf{k} -paths parallel to directions in which the unit cell contains two molecules (here, along the \mathbf{a}_1 direction in the model crystal), the band width is evaluated as the difference between the corresponding eigenstates at the Γ -point, considering the detailed evolution of the bands. This is again done for the sake of consistency, to account for the backfolding of the band caused by the doubling of the unit cell. More details on the evaluation of the band widths are contained in the SI.

Regarding the tight-binding fits, the functional form of the model function differs, depending on whether there are one or two molecules in the unit cell. For α -quinacridone with only a single molecule per unit cell it reads:

$$E(\mathbf{k}) = \varepsilon + \sum_j t_j \cdot e^{i\mathbf{k}\cdot\mathbf{R}_j} \quad (1)$$

Here ε denotes the on-site energy, t_j is the transfer integral for neighboring molecules along direction j and \mathbf{R}_j is the vector connecting the central molecule with the respective neighbor.

Due to the inversion symmetry of α -quinacridone, the two neighbors at \mathbf{R}_j and $-\mathbf{R}_j$ are equivalent, which results in identical transfer integrals t_j .

The equation becomes more complex, when the unit cell contains two inequivalent molecules,¹⁴ like in β - and γ -quinacridone and in the coplanar model system. It reads:

$$E(\mathbf{k}) = \frac{H_{AA}+H_{BB}}{2} \pm \sqrt{\frac{(H_{AA}-H_{BB})^2}{4} + |H_{AB}|^2} \quad (2)$$

Here, the indices A and B denote the inequivalent molecules present in the unit cell; H_{AA} and H_{BB} are terms describing the coupling between equivalent molecules in neighboring unit cells.

The couplings between inequivalent molecules, either in the same or in different unit cells, are included in the term H_{AB} . All these terms have the same functional form; only the neighbors considered in the sum are different:

$$H_{AA/BB/AB} = \sum_j t_{\mathbf{R}_j,AA/BB/AB} \cdot e^{i\mathbf{k}\cdot\mathbf{R}_{j,AA/BB/AB}} \quad (3)$$

In β - and γ -quinacridone and in the coplanar model system, for symmetry reasons H_{AA} , $t_{j,AA}$, and $\mathbf{R}_{j,AA}$ are the same as H_{BB} , $t_{j,BB}$, and $\mathbf{R}_{j,BB}$. The vectors $\mathbf{R}_{j,AB}$ differ from the $\mathbf{R}_{j,AA}$ and $\mathbf{R}_{j,BB}$ by the displacement vector between the two inequivalent molecules in the unit cell. To obtain the transfer integrals, one has to fit the above expressions to the energy eigenstates of the system within the entire first Brillouin zone. In passing, we note that increasing the number of inter-molecular interactions included in the tight-binding fits does not impact the values of transfer integrals determined already with fewer parameters, which is discussed in more detail

in Ref. 17. A list containing all inter-molecular interactions that have been included for the three quinacridone polymorphs and the coplanar model system can be found in the Supporting Information.

2.5 Determining the contributions to the bonding energy in the coplanar model crystal

A central element of the present manuscript is the analysis of the total energy of the systems (especially the total energy of the coplanar model crystal as a function of inter-molecular displacements). In this context it is relevant to analyze the origin of the observed differences via energy decomposition approaches. This is frequently done for finite-size systems and molecular dimers.^{34,62–71} In the present context we, however, primarily care about the 3D crystalline environment of the molecules. Therefore, we resorted to the recently developed “periodic energy decomposition analysis” (pEDA),^{68,72} which decomposes the interaction energy ΔE_{int} between two fragments into several well defined contributions.

$$\Delta E_{\text{int}} = \Delta E_{\text{Pauli}} + \Delta E_{\text{elstat}} + \Delta E_{\text{orb}} \quad (4)$$

The first is the quasi-classical electrostatic energy, ΔE_{elstat} , which considers the Coulomb interaction between the nuclei and electronic charge densities of the two fragments. This energy contribution also includes effects like charge penetration (i.e., the attractive interaction between the electron cloud of one sub-system and the nuclei of the other, which becomes relevant at small distances).^{66,73,74} The ΔE_{elstat} term is (nearly) always attractive due to the larger magnitude of electron-nuclei attraction in comparison to the repulsive terms – this is also found here. ΔE_{elstat} does not yet consider modifications of the charge densities of the fragments due to the interaction. The energetic cost/gain of these modifications is split into two terms: When

constructing a wavefunction of the joint system as a product of the eigenfunctions of the fragments, this new wavefunction needs to be normalized as well as antisymmetrized to obey the Pauli principle. The energetic cost for achieving that is termed Pauli repulsion energy, ΔE_{Pauli} . The last term arises from the final relaxation of the charge density to the self-consistent density of the combined system and determines the attractive orbital interaction energy, ΔE_{orb} . The final contribution to the interaction energy is the van der Waals attraction, which is calculated a posteriori, as described in sections 2.1 and 2.2. It has been shown recently, that the energy terms in the EDA analysis can be well compared to the results from symmetry-adapted perturbation theory analysis (SAPT) and lead to similar insights regarding the bonding situation.⁷⁵ Core advantage of the the pEDA analysis is that it considers the full periodicity of the crystalline environment.

The pEDA analysis is implemented in the ADF-BAND package,⁷⁶⁻⁷⁸ we thus employed that code (version 2018, r69431) for the energy decomposition in combination with the PBE functional, a TZ2P⁷⁹ basis set, a small frozen core, scalar relativistic effects in the ZORA approach, an SCF convergence criterion of 10^{-6} eV and 3D periodic boundary conditions. A Γ -centered 5 x 3 x 5 k-point grid was used after checking for convergence (see SI).

The crystal structures were visualized using Ovito⁸⁰ and the molecular orbitals by Avogadro.⁸¹

3. RESULTS AND DISCUSSION

3.1 Crystalline α -, β -, and γ -quinacridone.

The structures of the three established polymorphs of quinacridone are shown in Figure 2. Of the α -polymorph, two variants have been discussed (α^{I} and α^{II}),³⁵ where only the existence of α^{I} is undisputed. Thus, in the following, this phase will be denoted as α -quinacridone. The α -

and β -phases consist of H-bonded molecular stripes, which are not exactly planar, but exhibit small steps between the molecules. In β -quinacridone they, for example, amount to 0.35 \AA .³⁵ The fundamental difference between the two polymorphs is that in the α -phase all stripes run in the $\mathbf{a}_1+\mathbf{a}_2$ direction (perpendicular to the plane of projection in the right panel of Figure 2a), while in the β -phase they run in different directions in consecutive layers ($\mathbf{a}_1+\mathbf{a}_2$ and $\mathbf{a}_1-\mathbf{a}_2$). Consequently, α -quinacridone contains one and β -quinacridone two molecules in the unit cell. Nevertheless, in both cases the stripes are π -stacked in the \mathbf{a}_1 direction, which corresponds to the shortest vector between two neighboring molecules, whose π -systems overlap (c.f., grey arrow). For the γ -phase, the packing motif is fundamentally different (Figure 2c): While for the α - and β -phases each quinacridone molecule forms two H-bonds to each of its two neighbors (causing the formation of the stripes), in γ -quinacridone every molecule has a single hydrogen bond to four different neighbors. This gives rise to a “hunter fence” structure, as shown in the bottom panel of Figure 2c. Nevertheless, one can still identify a π -stacking direction (grey arrow).

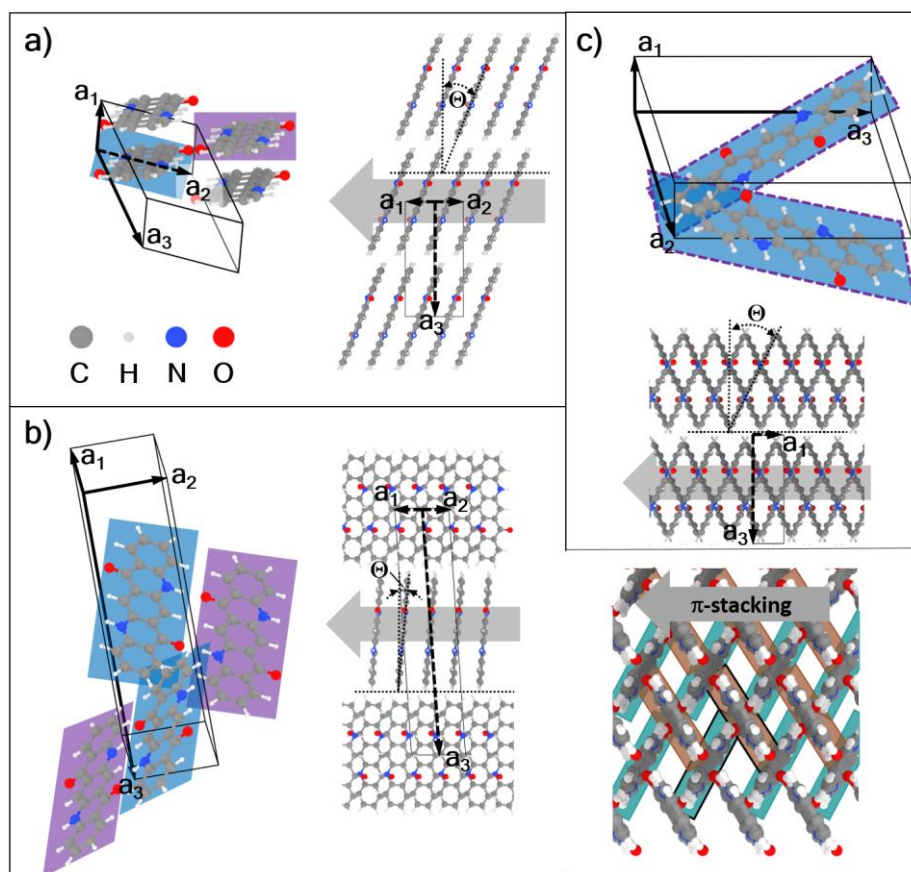


Figure 2. Crystal structures of the three quinacridone polymorphs. (a) left: view of the unit cell of α -quinacridone with the molecule in the original cell marked by a blue rectangle and the closest H-bonding partner marked by a purple rectangle; right: side view of the crystal structure with the viewing direction chosen such that the alignment of the H-bonded stripes is resolved most clearly. The π -stacking direction is indicated by a gray arrow. (b) left: unit cell of β -quinacridone; again, the blue rectangles mark the (in this case two) molecules in the unit cell and the closest H-bonding partners are highlighted in purple. The central panel again provides a side view, illustrating the alignment of the H-bonded stripes. In the right panel the viewing direction is perpendicular to the $(\mathbf{a}_1, \mathbf{a}_2)$ plane to illustrate that the π -stacking direction is the same for all layers (with molecules in different layers highlighted by the cyan and brown shading). (c) left: unit cell of γ -quinacridone containing two molecules, which are H-bonded to each other; right: side view illustrating the “hunter fence” arrangement of the molecules.

Of particular interest for the electronic couplings along the π -stacking direction (as the main topic of the present paper) is the displacement of the molecules along the short and long molecular axes in consecutive stripes. These displacements are summarized in Table 1. Consistent with the rather large inclination of the molecular stripes (Θ , see Figure 2) in the α -phase, this polymorph is characterized by a rather pronounced long-axis displacement (1.4 Å) and a smaller short-axis displacement (0.9 Å). Conversely, for β -quinacridone the long axis displacement is negligible (0.1 Å), while the short axis displacement amounts to 2.0 Å, which is more than twice as large as for the α -phase. For the γ -phase, due to the hunter fence arrangement of the molecules, the relative displacement of neighboring molecules is determined by the distance between the H-bonding sites on each molecule and by the equilibrium distance between the molecular backbones. Amongst the three different polymorphs, this results in the largest value of θ and, correspondingly, in the largest long-axis displacement of neighboring molecules (1.7 Å see Table 1). Concomitantly, the short axis displacement is the shortest of all polymorphs (0.7 Å).

Table 1. Displacements of neighboring molecules in π -stacking direction along their long and short molecular axes and inclination of the molecular planes relative to the quinacridone sheets, Θ , for α -, β -, and γ -quinacridone. Also, the energies per molecule relative to the most stable conformation (γ -quinacridone) are reported. Values which have been obtained employing the many-body dispersion correction scheme are given in brackets.

	long axis displacement / Å	short axis displacement / Å	inclination angle $\Theta / ^\circ$	relative energy / meV
α	1.4	0.9	21.5	+90 (88)
β	0.1	2.0	6.1	+5 (3)
γ	1.7	0.7	25.1	0 (0)

Energetically, using the TS van der Waals corrections we find that the α -phase is less stable than the γ -phase by 90 meV per molecule (see Table 1), while the total energies of β -quinacridone and γ -quinacridone are within 5 meV. This means that (within the numerical accuracy of our simulations) the latter two phases are isoenergetic despite their fundamentally different structures. These trends also prevail when employing the MBD scheme with energetic differences of 88 meV and 3 meV (for more details see Supporting Information). The above values do not contain vibrational energies and entropies. Nevertheless, it is interesting to compare the calculated trends to experimental observations: For example, Lüftner et al.⁶¹ observed the β -polymorph when growing quinacridone on Cu(111), while Paulus et al.³⁵ concluded that γ -quinacridone is most stable. They also successfully determined the structures of β - and γ -quinacridone, but found it impossible to grow large enough single crystals of the α phase for single-crystal diffraction experiments, which massively complicated the determination of its structure.³⁵ They also describe that the β - and γ -phases are stable and typically do not interconvert into each other. This is not the case for α -quinacridone, which may convert into the β - and γ -phases, preventing its commercial use.³⁵ All these findings are in line with the above-discussed trends in total energy.

Regarding the electronic structure of the quinacridone polymorphs, a comparison of the bands in the high-symmetry directions in reciprocal space for α -, β -, and γ -quinacridone is shown in the Supporting Information. The shapes of the bands are essentially the same independent of whether one employs the PBE or the HSE06 functional. Overall, the band dispersions are comparably small, ranging between 22 meV and 324 meV for the valence band and between 111 meV and 262 meV for the conduction band in the PBE calculations. These widths only somewhat increase for the HSE-calculated bands (see Table 2). Also the total band widths, W , characteristic of the entire volume of the first Brillouin zone, remain rather small varying

between 148 meV and 324 meV for the valence and between 252 and 345 meV for the conduction band (see Table 2). Interestingly, in all these cases (with the exception of the conduction band in ΓX direction) the band widths are largest for the β -polymorph and rather similar for α - and γ -quinacridone. Thus, for the three established quinacridone polymorphs, there is no apparent correlation between the total widths of the frontier bands and the energetic stability of the materials.

Table 2. Total band-widths, W , band-widths along ΓX , $W_{\Gamma X}$, and band widths for bands running parallel to the π -stacking direction (i.e., parallel to \mathbf{a}_1), W_{a_1} , for all 3 quinacridone polymorphs. The ΓX direction in reciprocal space is close to parallel to \mathbf{a}_1 . Additionally, transfer integrals in \mathbf{a}_1 direction calculated from tight-binding fits, t_{a_1} , and employing molecular dimers are shown. For the latter, we compare the results of ESD, t_{ESD} , and FO, t_{FO} , calculations. Note that although the H-bonded quinacridone stripes run in different directions in consecutive quinacridone layers in the β -polymorph, the π -stacking direction in all layers is given by \mathbf{a}_1 . (PBC) denotes results obtained in DFT calculations employing periodic boundary conditions, (TB) are values extracted from the corresponding tight-binding fits, and (dimer) refers to the results of dimer calculations. In addition to the results obtained with the PBE functional, for the sake of comparison we also show the values obtained employing the hybrid functional HSE for t_{ESD} and $W_{\Gamma X}$. A brief discussion of the HSE06 values for t_{FO} can be found in the Supporting Information

				α	β	γ
Valence Band	PBE	W / meV	(PBC)	152	324	148
		$W_{\Gamma X}$ / eV	(PBC)	22	324	82
		W_{a_1} / meV	(PBC)	15	324	76
		$ t_{a_1} $ / meV	(TB)	5	54	22
		$ t_{esd} $ / meV	(dimer)	4	43	20
		$ t_{fo} $ / meV	(dimer)	6	41	19
	HSE	$W_{\Gamma X}$ / meV	(PBC)	39	330	99
		$ t_{esd} $ / meV	(dimer)	6	44	24
Conduction Band	PBE	W / meV	(DFT)	252	345	263
		$W_{\Gamma X}$ / eV	(PBC)	129	111	262

		W_{a_1} / meV	(PBC)	100	111	262
		$ t_{a_1} / \text{meV}$	(TB)	18	31	53
		$ t_{\text{esd}} / \text{meV}$	(dimer)	17	21	30
		$ t_{\text{FO}} / \text{meV}$	(dimer)	10	19	32
HSE		$W_{\Gamma X} / \text{meV}$	(PBC)	135	112	297
		$ t_{\text{ESD}} / \text{meV}$	(dimer)	20	19	36

As far as the anisotropy of the resulting electronic coupling is concerned, a detailed analysis of the situation in α -quinacridone with a focus on differences between the H-bonding, van der Waals stacking, and π -stacking directions can be found in Ref [17]. Here, we are primarily concerned with transport along the π -stacking direction, \mathbf{a}_1 . Correspondingly, Figure 3 shows the valence and conduction bands of the three quinacridone polymorphs along a \mathbf{k} -path starting at the Γ point and running parallel to the \mathbf{a}_1 direction until the boundary of the Brillouin zone ($\Gamma \rightarrow A_1$). Again, the band widths are rather small, but more importantly, compared to the total band widths, there are even more significant differences between the three polymorphs, especially for the valence band: It is essentially flat for α -quinacridone parallel to \mathbf{a}_1 . Consequently, W_{a_1} (=15 meV) is by an order of magnitude smaller than the total band width. This is because in α -quinacridone the valence band along \mathbf{a}_1 is significantly narrower than, e.g., the band in the H-bonding direction ($\mathbf{a}_1 + \mathbf{a}_2$, i.e., along $\Gamma \rightarrow A_{12}$, also shown in Figure 3). W_{a_1} is intermediate for γ -quinacridone (76 meV) and largest for β -quinacridone (324 meV, see also Table 2). In γ -quinacridone, W_{a_1} and W are actually identical, which indicates that in this system both, the maximum and the minimum of the band are found along $\Gamma \rightarrow A_1$. The same trend as for W_{a_1} is also found for transfer integrals between molecules displaced by \mathbf{a}_1 . This happens independent of whether one considers the values obtained from the tight binding fits, t_{a_1} , or from dimer calculations⁸² within the electronic splitting in dimers approach, t_{ESD} , or performing fragment orbital simulations, t_{FO} (see Table 2). Minor deviations between transfer integrals extracted from the tight-binding fits and obtained from dimer calculations are

primarily attributed to the conceptual differences between the two approaches, especially the fact that the crystalline environment is only accounted for when determining t_{a1} . The latter is particularly relevant for quinacridone, where a dimer calculation misses the change in conjugation due to the H-bond formation.⁸³

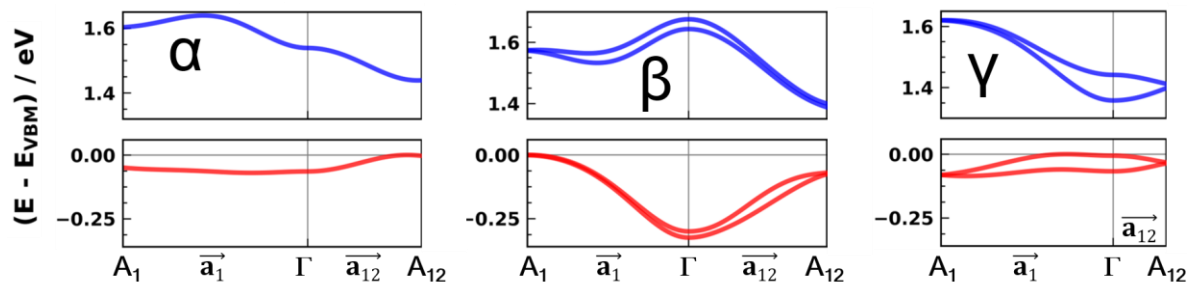


Figure 3. Electronic band structures of the three quinacridone polymorphs shown along k -paths originating at Γ and running parallel to the real space \mathbf{a}_1 and $\mathbf{a}_1+\mathbf{a}_2$ directions until the Brillouin zone boundaries. Energies are plotted relative to the valence-band maximum.

The situation is somewhat more involved for the conduction bands, as for the α - and β -polymorphs they display a distinctly non-cosine shape, which is a clear evidence for “higher-frequency” components (i.e., transfer integrals beyond the nearest neighbors) playing a significant role.¹⁷ Indeed, an analysis of the tight-binding fits shows that the corresponding transfer integrals can be associated with next-nearest neighbor couplings (t_{2a1}). This we attribute to “superexchange-like” type interactions (for a more in depth discussion of this aspect in α -quinacridone see Ref [17]). Correspondingly, the direct correlation between band widths and transfer integrals is lost for the conduction bands. For example, t_{a1} is nearly twice as large for β -quinacridone as for α -quinacridone, although the associated band widths are very similar. While this complicates the situation when analyzing electron transport, here we are mostly concerned with occupied bands, as only their properties can have an impact on the total energy of the system.

When comparing the results of the PBE and HSE simulations we find that consistent with the similar band structures calculated in both cases, the band widths are also very similar. Furthermore, also the dimer-calculated transfer integrals when employing the ESD approach turn out to be quite robust against changing the exchange correlation functional.

3.2 Properties of the coplanar model system of quinacridone

The above-described results for the three quinacridone polymorphs do not show a clear correlation between total energy and transfer integrals or band width. Therefore, it is useful to analyze a model system, whose properties can be assessed in a more systematic way. Such a system is found in the coplanar model crystal derived from α -quinacridone, which is shown in Figure 1 and whose structure is discussed in detail in the methods section. Based on this model crystal, we will not only analyze the dependence of the electronic couplings on the intermolecular displacements, but will primarily search for correlations between, on the one hand, transfer integrals and band widths and, on the other hand, the total energy of the system. Moreover, we will analyze the various ingredients to the total energy in order to clarify, whether specific interactions exist that try to force molecular crystals towards configurations with low electronic couplings. As a first step in this quest, Figure 4 shows how the total energy, the van der Waals energy, and the total width of the valence band of the coplanar model crystal depend on the displacement of neighboring sheets.

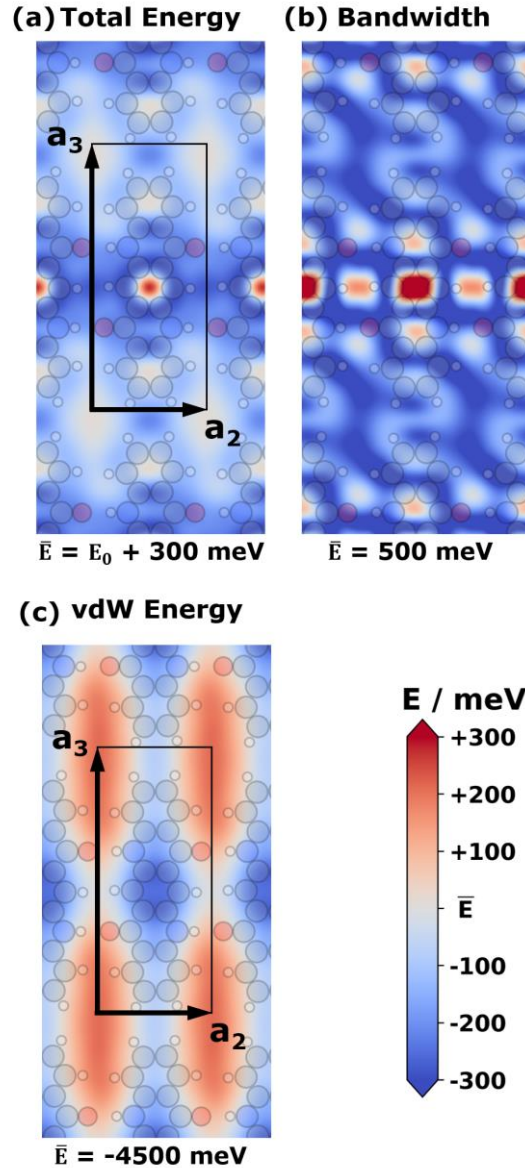


Figure 4. PBE calculated total energy (a), van der Waals energy derived from the TS approach (b) and total width of the valence band (c) as a function of the displacement of neighboring sheets. The position in the graph denotes the position of the center of a molecule in the second layer within the unit cell relative to the first layer, whose structure is indicated in the plot. All energies are given relative to an average value of the respective energy, which is specified below each of the panels. The total energy plot is additionally offset by E_0 , which is the value for the lowest-energy structure. As far as the total band width is concerned, the covered range is somewhat larger than indicated by the color bar, as its value varies between 140 meV and 1100 meV.

The data in Figure 4 show that the total energy is maximized for the cofacial, zero displacement situation. Notably, all local maxima of the total energy are found for displacements along the long molecular axis, with the exception of the situation in which the quinacridone sheets are displaced by half the unit cell lengths simultaneously in \mathbf{a}_2 and \mathbf{a}_3 directions. This maximum can be associated with a reduced van der Waals attraction between the sheets due to the minimized van der Waals contact area in this configuration (see Figure 4c). The energetically best configurations are also found in the vicinity of structures displaced either along the long or along the short molecular axis (the global maximum occurs for a long-axis displacement of 1.5 Å and a simultaneous minor short-axis displacement of 0.3 Å). A similar behavior is observed for the most pronounced maxima of the total band widths in Figure 4b (with by far the largest band width for the cofacial, zero-displacement structure). This suggests that for a more in depth and more quantitative discussion, it is useful to primarily analyze displacements either along the long or along the short molecular axis.

Displacing consecutive molecular sheets along the long molecular axis in coplanar quinacridone – quantifying the electronic coupling.

The results for the long-axis displacement are shown in Figure 5. Here, as a first step, we compare the trends for the most relevant parameters used in Table 1 to quantify the strength of the electronic coupling in order to determine whether a single one of them will be sufficient for the further discussion. Such a test is advisable, as when analyzing the anisotropy of coupling parameters in α -quinacridone, relevant deviations between, for example, band widths and transfer integrals have been observed.¹⁷ The results for the (valence-band related) transfer integral between displaced molecular dimers obtained with the fragment orbital approach, t_{FO} , are shown in Figures 5a. They display an evolution reminiscent of the observations for rubrene,²⁸ anthradithiophene,²⁴ or sexithienyl:²⁶ There is a pronounced maximum for zero

displacement, subsequently t_{FO} crosses the zero line, reaches a negative maximum and then crosses the zero line again.

Before comparing these trends to those for the corresponding transfer integral(s) obtained via the tight-binding fit, two technical aspects need to be mentioned: First, it is not possible to extract the sign of the transfer integral describing the coupling between the two inequivalent molecules in the unit cell, t_{AB} , (see Figure 1) unambiguously. This is due to symmetry reasons and the functional form of the tight-binding band structure for two molecules in the unit cell. All that can be determined is, whether the signs of t_{AB} and t_{AB-a3} (see Figure 1) are the same or not. Second, the band dispersion in the \mathbf{a}_1 direction in the coplanar model crystal does not depend on these two transfer integrals individually but is only determined by their sum. Thus, in Figure 5b this sum, $t_{AB}+t_{AB-a3}$, is shown with the sign chosen such that it is consistent with that of t_{FO} . These aspects are discussed in detail in the Supporting Information, where also the values of the individual transfer integrals t_{AB} and t_{AB-a3} are plotted. In this context it should also be noted that especially for small displacements the contribution from t_{AB-a3} is negligible ($|t_{AB-a3}| < 5$ meV for displacements < 2.6 Å and $|t_{AB-a3}| < 20$ meV for displacements < 4.7 Å). Thus, the plot in Figure 5b for small and intermediate displacements mostly reflects the evolution of t_{AB} . As far as the overall trends are concerned, there are only minor deviations between t_{FO} and $t_{AB}+t_{AB-a3}$ concerning the magnitude of the maxima at higher displacements and their exact positions. We attribute these differences mostly to changes in the orbital structure arising from the interaction between the molecules in the actual crystalline environment.

To more easily compare the trends for the transfer integrals to those for the band widths, we also show the evolution for $|t_{AB}+t_{AB-a3}|$ in Figure 5b as a dashed red line. This reveals a close to perfect agreement between the evolutions of $|t_{AB}+t_{AB-a3}|$, the total width of the valence band, W , and the width of the valence band along a path starting at the Γ point and running along \mathbf{a}_1 , $W_{\mathbf{a}_1}^{VB}$. The latter data are shown in Figure 5c. In passing, we note that $W_{\mathbf{a}_1}^{VB}$ is close to zero at

the displacements corresponding to zero-crossings of the transfer integrals, while this is not the case for W . This is simply due to the fact that for W also the band widths along other paths (e.g. parallel to the H-bonding direction) count, which are largely unaffected by the displacement of the quinacridone sheets.

As far as the employed functional is concerned, using HSE leads to an increase of the maximum values of W_{a1}^{VB} by ca. 100 meV which corresponds to a relative change of $\sim 12\%$. Despite the quantitative differences, switching the functional does not affect the shapes of the bands nor the evolution of t_{FO} with the displacement (see Supporting Information).

Considering the above comparison and the overall qualitative agreement between all quantities used to determine the displacement-dependent trends in the electronic coupling, in the following we will restrict the analysis primarily to PBE-calculated band widths as the most straightforwardly accessible parameters for the actual crystals.

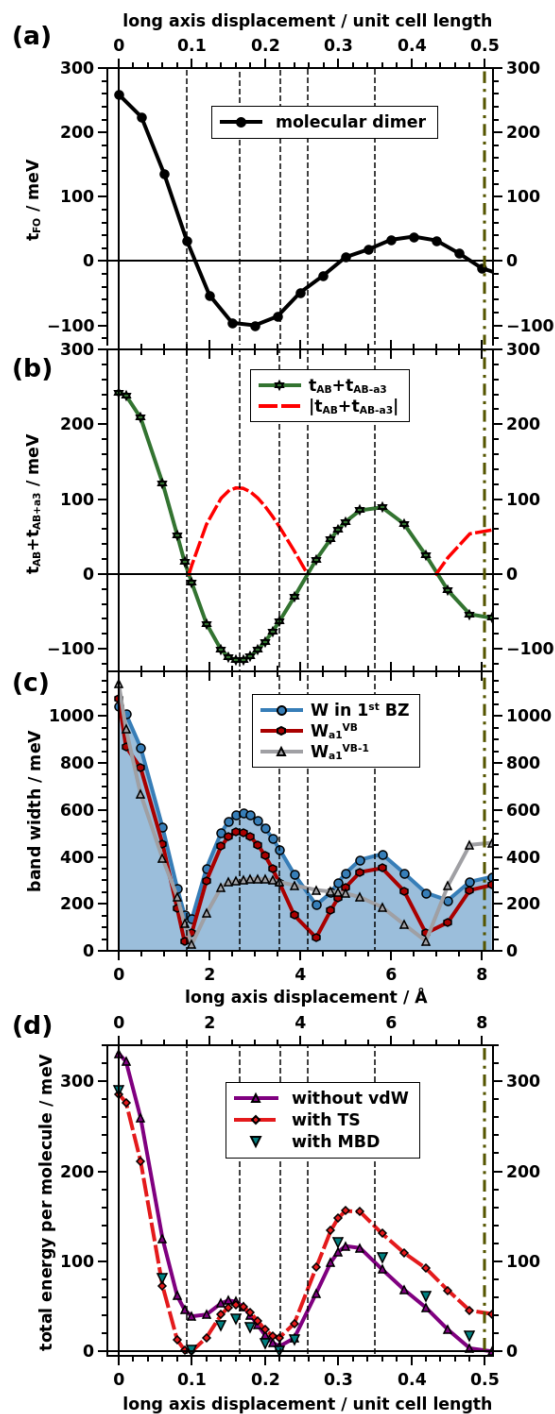


Figure 5. Dependence of the PBE-calculated electronic coupling, (a)-(c), and the energy per molecule, (d), on the long-axis displacement for quinacridone. The values in (b)-(d) have been calculated for the coplanar model crystal and those in (a) for the corresponding molecular dimer. The transfer integrals in (a) have been calculated via the fragment orbital method. Employing the energy splitting in dimer method yields the same results, as shown in the

Supporting Information. In (b) the sum of the tight-binding derived transfer integrals to the two neighboring molecules in the stacking direction is shown (for details see main text) and (c) contains the total band width of the valence band sampled over a tight k -point grid (area shaded in blue) as well as the widths of the valence band (VB, derived from the molecular HOMO) and the next lower band (VB-1, derived from the HOMO-3) for the k -path running from the Γ -point to the Brillouin-zone boundary in a direction parallel to \mathbf{a}_1 . In (d) the total energies per molecule including and disregarding TS and MBD -type van der Waals interactions are shown relative to the minimum energy obtained for the long-axis displacement-. The dotted vertical lines are guides to the eye, while the dash-dotted line denotes a shift by half of the unit-cell length. On the vertical axes, the displacements are given in \AA as well as in multiples of the corresponding unit-cell length.

Displacing consecutive molecular sheets along the long molecular axis in coplanar quinacridone – evolution of the total energy.

A central observation for the present study is made when comparing the evolution of the band widths with that of the total energy of the system, shown in Figure 5d. Especially, for small displacements, their evolutions run parallel (c.f., Refs. [34,65]), as can be seen comparing Figure 5d with Figures 5a-c. In detail, as already mentioned in the discussion of Figure 4, the largest band width and the highest total energy are found when not displacing consecutive quinacridone sheets. Moreover, the total energy reaches its minimum for a total displacement of ca. 1.5 \AA , where also the electronic coupling is minimized. This suggests that there is a fundamental driving force steering the crystal towards a structure with a minimized electronic coupling. In this context it is important to stress that the unfavorable situation for zero displacement is not primarily the consequence of arranging the polar carbonyl and amine

groups on top of each other, as a similarly pronounced energetic maximum is observed when flipping the molecules in the second layer by 180° placing the amines on top of the ketones. The origin of the above-mentioned driving force minimizing the band-width can rather be traced back to exchange repulsion, as stressed in Ref. [34] and discussed for molecular dimers of acenes employing symmetry-adapted perturbation theory.⁶⁵ Qualitatively, the variation of the total energy with displacement can be understood from the following consideration: When the orbitals of two molecules overlap, bonding and antibonding linear combinations are formed, where the bonding one is stabilized less than the antibonding one is destabilized. As the energies of the occupied bands (orbitals) enter into the expression of the total energy, wavefunction overlap involving fully occupied orbitals, thus, results in a repulsive contribution, with the effect being particularly pronounced for large energetic splittings and, correspondingly, strong electronic couplings.

To ensure that such a destabilization of the structures by large transfer integrals is indeed a consequence of the modification of the wavefunctions due to the interaction between neighboring quinacridone sheets, we performed a periodic energy decomposition analysis, as described in section 2.5 taking the two quinacridone sheets associated with the two molecules in the unit cell as the two fragments for the analysis. The resulting contributions to the electronic interaction energy, ΔE_{int} , (not comprising long-range van der Waals interactions)^{68,72} are shown in Figure 6a relative to the values obtained for zero displacement (where the latter are listed in the figure caption). One clearly sees that the evolutions of the Pauli repulsion energy, ΔE_{Pauli} , and the orbital interaction energies, ΔE_{orb} , both directly follow the trend for the total energy. I.e., the modification of the wavefunctions in the interacting system is indeed responsible for the destabilization of the model system at large transfer integrals. This shows that for the present system attractive interactions, e.g., due to charge penetration^{66,73} are insufficient to overcome exchange repulsion. At this stage it should also be mentioned that

although ΔE_{Pauli} displays an oscillatory behavior, its absolute value always remains large (> 1.5 eV), consistent with what Sutton et al. observed for the exchange repulsion, when analyzing molecular dimers.³⁴

The impact of the electrostatic interaction energy between the sheets, ΔE_{elstat} , on the relative stability of different geometries is less pronounced. It somewhat destabilizes the zero-displacement situation and stabilizes the displacement at which the total energy reaches its second maximum as well as a shift by half of the unit cell. Overall, the electrostatic energy, however, does not severely impact the observed trends.

As far as the long-range van der Waals contributions are concerned, several conclusions can be drawn. When considering the absolute values of the energy contributions (see caption of Figure 5), it becomes evident that the van der Waals attraction is the force that results in the formation of the crystal, as it is the only attractive interaction that is large enough to overcome Pauli repulsion. Concerning the relative stability of different displacements, the van der Waals contribution does not change the general shape of the total energy curve (see Figure 5d). It, however, determines the relative stability of the two minima at displacements of 1.5 Å and 2.5 Å. Van der Waals interactions stabilize smaller displacements. Thus, for the TS van der Waals correction the first minimum is the lower one, although ΔE_{int} and the total energy excluding van der Waals corrections (Figure 5d) are smallest at the second one. The trend is also observed when using the MBD correction, although there the stabilization of the first minimum is smaller such that it becomes essentially isoenergetic to the second one.

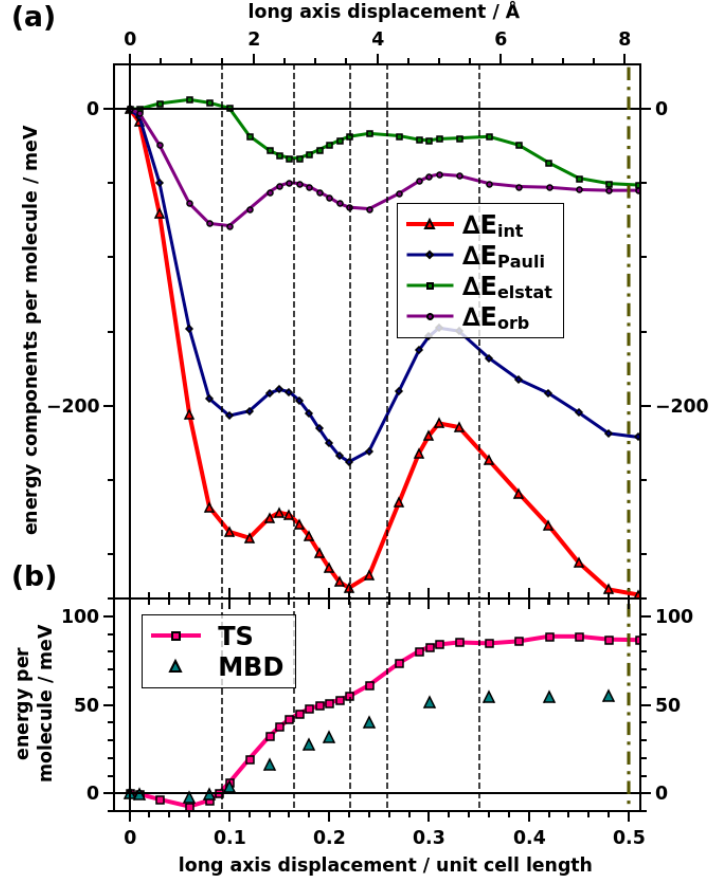


Figure 6: (a) PBE-calculated relative evolution of the electronic interaction energy, ΔE_{int} , (excluding a-posteriori van der Waals corrections) and its components (Pauli repulsion energy, ΔE_{Pauli} , orbital interaction energy, $\Delta E_{orbital}$, and electrostatic energy, ΔE_{elstat} , as a function of the long-axis displacement in a coplanar quinacridone model crystal). The energies are given relative to the zero-displacement situation. For the latter the following absolute values (per molecule) are obtained: $\Delta E_{int} = 407 \text{ meV}$, $\Delta E_{Pauli} = 870 \text{ meV}$, $\Delta E_{elstat} = -343 \text{ meV}$, $\Delta E_{orbital} = -120 \text{ meV}$. As the minima for different quantities are found at different displacements, aligning them relative to the energetic minima as in Figure 5 is not advisable, as this would obscure their additive character. (b) Evolution of the TS and MBD van der Waals correction energies with displacement. At zero displacement, the following absolute values (per molecule) are obtained: $\Delta E_{vdW,TS} = -2375 \text{ meV}$ and $\Delta E_{vdW,MBD} = -2651 \text{ meV}$.

Returning to the comparison between the band widths of the valence band and the total energy, the question arises, why the parallel evolution of the two quantities in Figure 5 does not prevail for larger displacements and why the one-to-one correlation between band width and total energy is also lost for most regions of Figure 4. We attribute this to the contribution of lower-lying occupied electronic bands (occupied orbitals for molecular systems). These do not impact charge transport per se, as electrons will always accumulate in the conduction band and holes in the valence band, but their contribution to the total energy is as important as that of the valence band.

As shown in Figure 7, there are various occupied bands that, for zero displacement, display widths comparable to that of the valence band. Of the bands we analyzed, this applies to all π -bands (red bars in Figure 7). Only for the 2nd and 3rd band below the valence band the widths are about one order of magnitude smaller, which is a consequence of their σ -character (black bars in Figure 7). The latter suggests that the interaction between σ -electrons has only a minor impact on the relative stability of certain displaced structures.

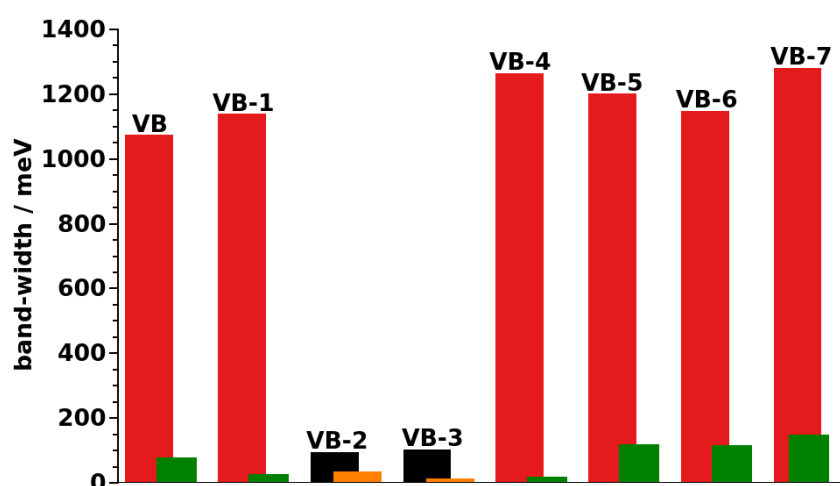


Figure 7: PBE-calculated bandwidths of the highest occupied bands of the coplanar quinacridone model crystal, evaluated as the splitting of the backfolded bands at the Γ point.

π -bands are denoted by red and green and σ -bands by black and orange bars. The widths were evaluated for zero displacement (red and black bars) and for a displacement of 0.1 times the length of the unit cell along the long molecular axis (green and orange bars).

The widths of all bands drop dramatically, when displacing consecutive quinacridone sheets by a tenth of the unit-cell length (see green and orange bars in Figure 7). This rationalizes the parallel evolutions of the valence-band width and the total energy for small displacements. Notably, although the band widths of all considered bands becomes very small at a displacement of one tenth of the unit cell, the absolute value ΔE_{Pauli} remains sizable (663 meV; i.e., larger than its variation with displacement in Figure 6).

As far as the evolution of the total energy at larger displacements is concerned, the varying nodal structures of the molecular orbitals forming the lower-lying bands (see Supporting Information) result in different trends for the band widths at larger displacements such that they no longer follow the valence band. This is exemplarily shown for the second-highest band (VB-1) in Figure 5c. It eventually causes the differences in the positions of the extrema in the valence band width and the total energy observed in Figure 5 for large displacements.

Short axis displacements in the coplanar quinacridone model crystal.

As mentioned above (cf., Figure 4), additional minima in the total energy and maxima of the band widths are found for displacing the quinacridone sheets along the short molecular axes. The resulting evolutions of the band widths and energies are shown in Figure 8. Again, the band width is maximized for zero displacement, drops sharply reaching a pronounced minimum for a short-axis displacement around 1.8 Å (corresponding to a quarter of the unit cell-length in that direction) and then rises again (Figure 8a). The sharp drop at small displacements is again accompanied by a pronounced drop in the total energy (Figure 8b). For

displacements of more than a quarter of the unit-cell length, the evolution of the total energy becomes very shallow. This implies that minor modifications in the interaction could easily change the position of the minimum, which would at the same time massively change the electronic coupling and the band width. In fact, even in our simulations the exact position of the minimum depends on the employed van der Waals correction (see Figure 8b).

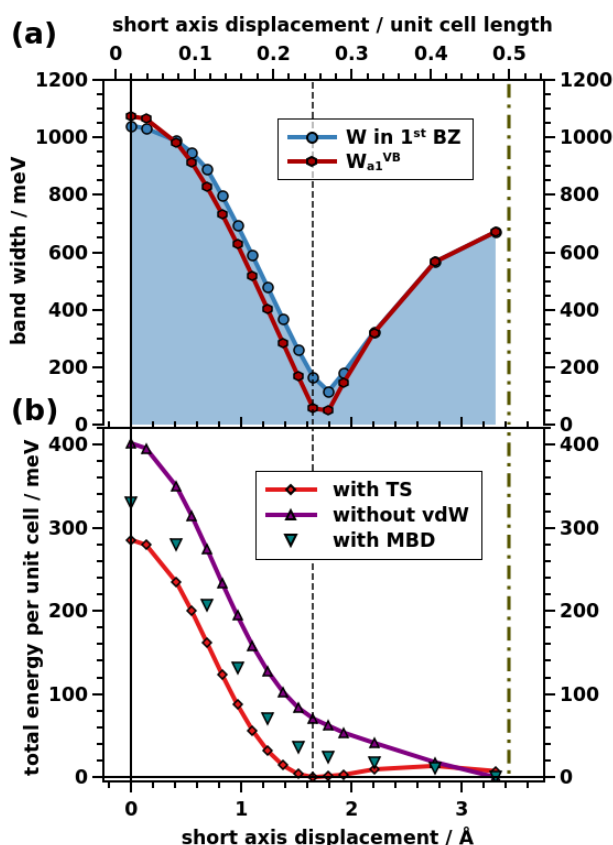


Figure 8. Dependence of the band widths, (a), and the energies per molecule, (b) on the short-axis displacement for the coplanar quinacridone model crystal. (a) contains the total band width of the valence band sampled over a tight k -point grid (area shaded in blue) as well as the widths of the valence band (VB, derived from the molecular HOMO) and the next lower band (VB-1, derived from the HOMO-3) for the k -path running from the Γ -point to the Brillouin-zone boundary in a direction parallel to \mathbf{a}_1 . In (b) the total energies per molecule including and disregarding van der Waals interactions are shown relative to the minimum

energy obtained for the short-axis displacement. The dotted vertical line is a guide to the eye, while the dash-dotted line denotes a shift by half of the unit-cell length. On the vertical axes, the displacements are given in Å as well as in multiples of the corresponding unit-cell length.

Performing an energy decomposition in analogy to the previous section reveals that electrostatic as well as van der Waals interactions favor small displacements (Figure 9). Their impact is, however, insufficient for dominating the overall evolution. Thus, again especially Pauli repulsion is responsible for the sharp drop in energy for displacements between zero and a quarter of the unit-cell length. At larger displacements it essentially compensates the evolutions of the electrostatic, the van der Waals, and the orbital interaction energies, which results in the very shallow area of the potential energy surface. The observation that in this displacement region ΔE_{Pauli} does not follow the evolution of the valence band width is again attributed to different nodal structures of other occupied orbitals.

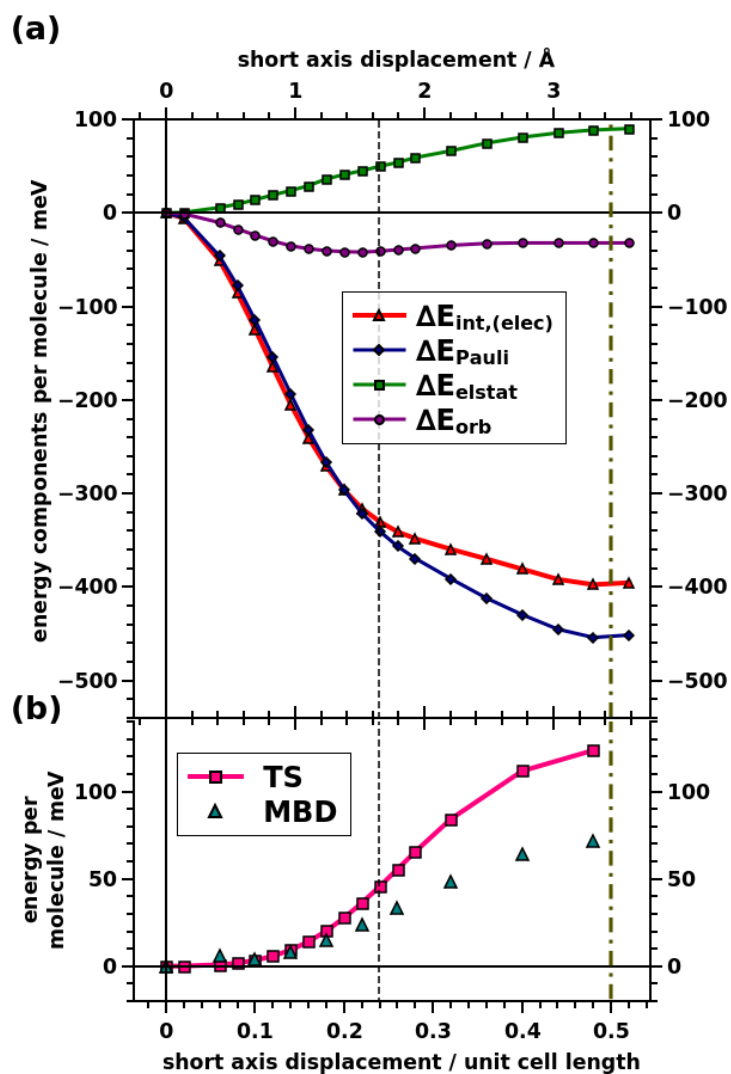


Figure 9. (a) PBE-calculated evolution of the electronic energy, ΔE_{int} , (excluding a-posteriori van der Waals corrections) and its components (Pauli repulsion energy, ΔE_{Pauli} , orbital interaction energy, $\Delta E_{\text{orbital}}$, and electrostatic energy, ΔE_{elstat}) as a function of the long-axis displacement in a coplanar quinacridone model crystal. The energies are given relative to the zero-displacement situation. (b) Evolution of the TS and MBD van der Waals correction energies with displacement.

Implications for the situation in α -, β -, and γ -quinacridone.

The structure of the α -polymorph is dominated by a displacement of neighboring quinacridone molecules along the long molecular axis (see Table 1). Intriguingly, this displacement amounts to 1.4 Å, which is very close to the zero-crossing of the transfer integrals for the model crystal upon long-axis displacement (at 1.5 Å). It also coincides with the minimum in total energy for this displacement. I.e., in α -quinacridone one observes a situation, where minimizing the energy also results in a vanishing transfer integral for the valence band. Interestingly, the calculated global energy minimum according to Figure 4 comprises a short-axis displacement of 0.3 Å (vide supra), which is well consistent with the experimental fact that the actual structure of α -quinacridone not only comprises a long- but also a smaller short-axis shift of the molecules (see above).

For β -quinacridone, the displacement along the short molecular axis dominates. For this direction, the coplanar crystal displays a very shallow minimum of the total energy, which does not necessarily coincide with the minimum in the electronic coupling for the valence band (see above). This suggests that even minor modifications in the crystal structure could easily result in situations with increased electronic couplings. This indeed is the case for β -quinacridone, where the equilibrium structure is characterized by a short-axis displacement of 2.0 Å, which is distinctly larger than the displacement of 1.6 Å representing the minimum band-width situation. This rationalizes the sharp increase of the electronic coupling in β -quinacridone compared to the α -phase (see Table 2).

The situation changes fundamentally in γ -quinacridone. Here, the total energy curve in Figure 5 is only of limited relevance due to the fundamentally different bonding motif in this polymorph, where the equilibrium displacement is strongly impacted by the positions the H-bonding sites and the equilibrium distance between two consecutive quinacridone planes (see section 3.1). This explains the increase of the long-axis displacement by 0.3 Å compared to the α -phase, which in turn results also in a larger band width consistent with the data in Table 2.

3.3 Molecular displacements, band widths, and total energies for a coplanar pentacene model crystal.

In order to highlight the general validity of the above considerations, we performed analogous simulations for a coplanar pentacene model crystal. As shown in Figures 10 and 11, this yields similar trends as in the quinacridone case.

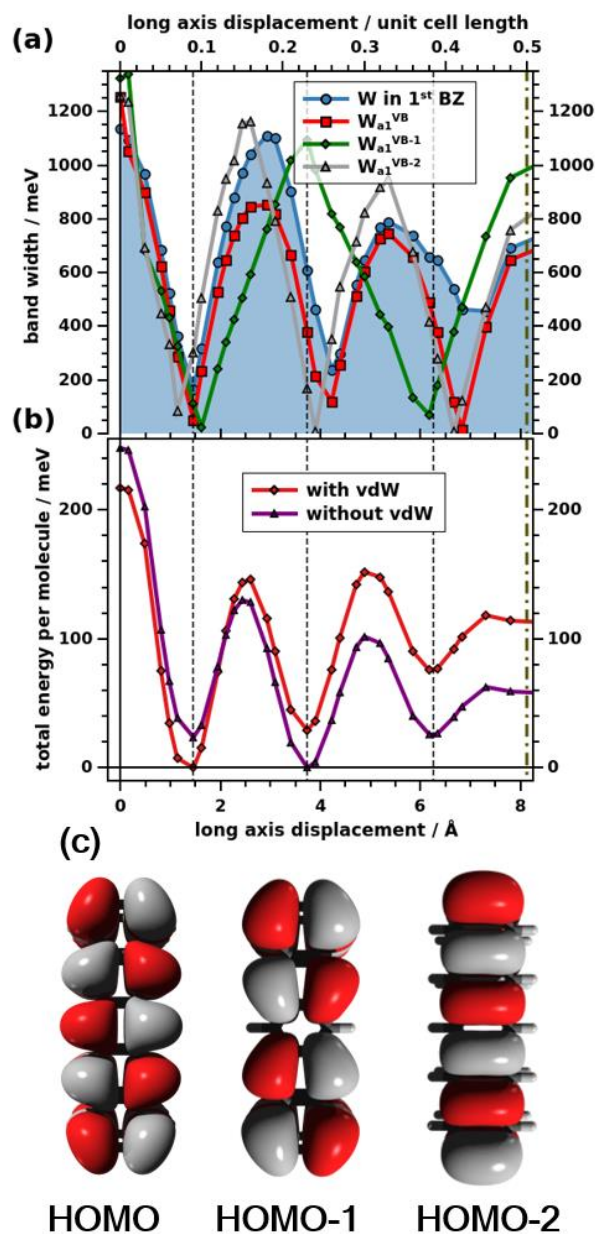


Figure 8. (a): Dependence of the band widths, on the long-axis displacement for the coplanar pentacene model crystal. The total band width of the valence band sampled over a tight k -point grid (area shaded in blue) as well as the widths of the valence band (VB, derived from the molecular HOMO) and the next two lower bands (VB-1, derived from the HOMO-1 and VB-2, derived from the HOMO-2) for the k -path running from the Γ -point to the Brillouin-zone boundary in a direction parallel to \mathbf{a}_1 are shown. The values of W following the definition of the quantity in the Methods section underestimate the actual situation for small displacements.

The reason for that is that there the band widths become so large that several valence bands overlap and the PBE calculated band gap vanishes (the corresponding band structure is shown in the Supporting Information). In (b) the total energies per molecule including and disregarding van der Waals interactions are plotted relative to the minimum energy obtained for long-axis displacement. The dotted vertical line is a guide to the eye, while the dash-dotted line denotes a shift by half of the unit-cell length. On the vertical axes, the displacements are given in Å as well as in multiples of the corresponding unit-cell length. Panel (c) contains isodensity plots of the three highest occupied molecular orbitals of pentacene.

For the long-axis displacement, the total valence band width again displays a pronounced succession of maxima and minima, where for short displacements there is a near perfect agreement of the trend with that observed for the total energy. This correlation is once more lost for larger displacements, which also here can be rationalized by the impact of lower-lying strongly dispersing occupied bands. In fact, as far as the latter aspect is concerned, pentacene serves as a particularly instructive example.: As shown in Figure 10c, the molecular HOMO-1, which in the crystal forms the band directly below the valence band, has a smaller number of nodal planes perpendicular to the long molecular axis than the molecular HOMO (forming the valence band). Consequently, the relative displacements between consecutive minima in the band width are larger. Conversely, for the molecular HOMO-2 (and the associated band in the crystal) with an increased number of nodal planes, the number of minima increases.

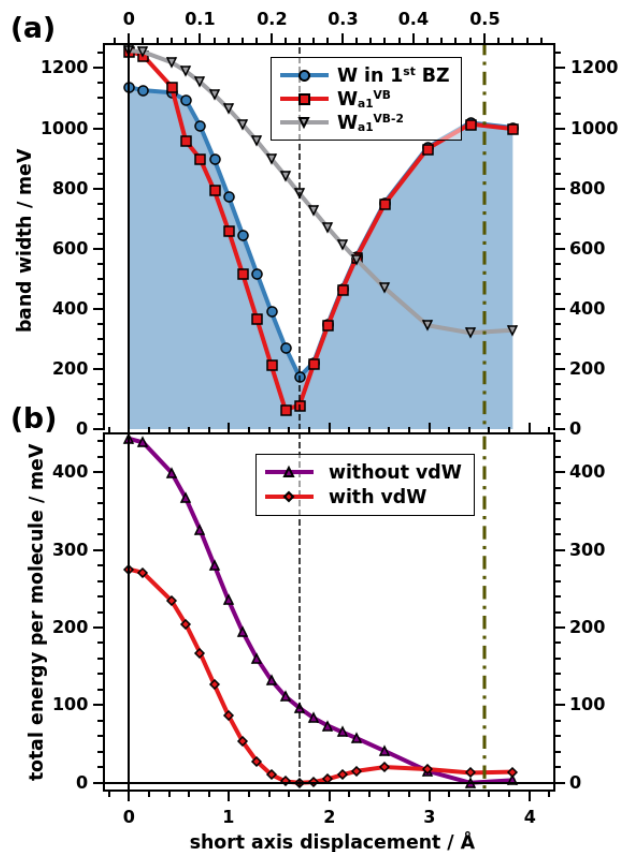


Figure 11. (a): Dependence of the band widths, on the short-axis displacement for the coplanar pentacene model crystal. The total band width of the valence band sampled over a tight k -point grid (area shaded in blue) as well as the widths of the valence band (VB, derived from the molecular HOMO) and a the VB-2 (derived from the HOMO-2) for the k -path running from the Γ -point to the Brillouin-zone boundary in a direction parallel to \mathbf{a}_1 are shown. The evolution for the VB-1 is not contained in the plot, as it follows that of the VB. The values of W following the definition of the quantity in the Methods section underestimate the actual situation for small displacements. The reason for that is that there the band widths become so large that several valence bands overlap and the PBE calculated band gap vanishes (the corresponding band structure is shown in the Supporting Information). In (b) the total energies per molecule including and disregarding van der Waals interactions are plotted relative to the minimum energy obtained for short-axis displacement. The dotted vertical line is a guide to the

eye, while the dash-dotted line denotes a shift by half of the unit-cell length. On the vertical axes, the displacements are given in Å as well as in multiples of the corresponding unit-cell length.

As far as the short axis displacement is concerned, the overall trends are again similar to the situation in the coplanar quinacridone model crystal (see Figure 9). Particularly instructive in the pentacene case is again the evolution of the band widths for deeper-lying bands, in particular the VB-2 (derived from the molecular HOMO-2). There, due to the absence of a nodal plane perpendicular to the short molecular axis, the associated band-width reaches its minimum only, when the sheets are displaced by half the inter-pentacene distance. I.e., they occur at twice the displacement for the minima of the VB and VB-1 (where the evolution latter essentially coincides with that of the valence band and, therefore, is not shown).

4. CONCLUSIONS

In the present work, we have examined the interplay between crystal packing, i.e. the relative stability of certain crystal structures, and transport relevant parameters for organic semiconductor crystals relying mostly on the instructive example of quinacridone. Comparing the electronic coupling in the three established, stable polymorphs of quinacridone, we find pronounced differences for the transfer integrals and band widths, which, however, do not correlate with the relative energies of the three structures. This prompted us to analyze a coplanar quinacridone model crystal, which allows relating various parameters characterizing the inter-molecular electronic coupling (like band widths and transfer integrals) to the relative displacements of the quinacridone sheets. Even more importantly, as we simulate these displacements in a 3D periodic, crystalline environment, it is possible to correlate the evolution of the electronic coupling in the valence band with the energetic stability of specific

configurations. For the sake of comparison, similar studies are performed for an analogous pentacene-based model system. These studies allow a number of conclusions: The largest band width in both systems are observed for a cofacial, zero-displacement arrangement of the molecules. This configuration is, however, destabilized by Pauli repulsion and orbital rehybridization involving all electrons in the occupied π -bands. Consequently, there is a general driving force pushing the crystals towards a situation with reduced electronic couplings. This, for example, explains the particularly small transfer integrals in the π -stacking direction of α -quinacridone. For small displacements, one even observes a direct correlation between the total energy of a configuration and the width of the valence band;³⁴ i.e., the smaller the width of the valence band becomes the more a structure is stabilized. Thus, for realizing high-mobility materials, one cannot rely on the intrinsic interactions driving the self-assembly of the π -conjugated backbones. Instead one has to exploit, e.g., steric effects induced through chemical substitutions.^{34,84–86} This is done, for example in the cases of rubrene^{28,65,87} or TIPS-pentacene,⁴⁰ where recently efforts have been undertaken to vary packing and displacements by carefully tuning the substituents.^{62,88} Alternative strategies for overcoming exchange repulsion comprise, e.g., heteroatom substitution and the inclusion of halogens in the periphery of the conjugated core as discussed comprehensively in Ref. [34].

Interestingly, the direct correlation between electronic coupling in the valence band and total energy is lifted for larger displacements both in the long- and short-axis directions due to the different nodal structures of lower-lying π -bands. This means that for structures more strongly displaced along the long molecular axis, a much smaller external stimulus (e.g., through substituents) should be enough for realizing large couplings in the valence band. Even more promising is to extrinsically control the short-axis displacement. In that case, a rather shallow local minimum in total energy as a function of the displacement is observed, as there the detrimental exchange repulsion due to the valence band is more readily overcome by lower-

lying bands derived from orbitals with fundamentally different nodal structures. This implies that with only minor modifications in the inter-molecular interactions, one should be able to significantly modify the relative arrangement of the molecules, which would then massively change the width of the frontier bands. In fact, this is to a certain extent already realized in β -quinacridone, where it results in an increase of the band width in π -stacking direction by an order of magnitude compared to the α -phase.

ASSOCIATED CONTENT

The supporting information contains additional methodological details including a specification of the used PAW potentials, a detailed specification of the basis set used in the FHI-aims simulations, a description of the geometry optimization of the coplanar model crystal, a summary of how band-widths have been calculated, a list of neighbors considered in the tight-binding fits, a description of complications arising for transfer integrals between successive quinacridone sheets in the coplanar model system, considerations regarding the stability of the tight-binding fit, data on the convergence of the k-point grid, and data on the uncertainty of the machine-learning model. Additionally, data on the impact of the used van der Waals correction and functional on band and orbital energies and total energies of the system are provided. Finally, the supporting information also contains information on H-bonding energies and distances, the calculated band structures of the quinacridone polymorphs along the high symmetry directions, additional information on deeper-lying bands and orbitals.

AUTHOR INFORMATION

ORCID

Christian Winkler 0000-0002-7463-6840

Andreas Jeindl 0000-0002-2436-0073

Ralf Tonner 0000-0002-6759-8559

Egbert Zojer 0000-0002-6502-1721

Corresponding Author

egbert.zojer@tugraz.at

Author Contributions

The manuscript was written through contributions of all authors. All authors have given approval to the final version of the manuscript.

Funding Sources

TU Graz Lead Project “Porous Materials at Work” (LP-03).

Austrian Science Fund (FWF): P28631-N36.

Notes

Any additional relevant notes should be placed here.

ACKNOWLEDGMENT

The work has been financially supported by the TU Graz Lead Project “Porous Materials at Work” (LP-03). Additional financial support by the Austrian Science Fund (FWF): P28631-N36 is gratefully acknowledged. The computational results have been in part achieved using the Vienna Scientific Cluster (VSC3). C. Winkler thanks Gernot J. Kraberger for stimulating discussions. R. Tonner thanks the German Science Foundation (DFG) for funding via SFB 1083.

REFERENCES

- (1) Pope, M.; Kallmann, H. P.; Magnante, P. Electroluminescence in Organic Crystals. *J. Chem. Phys.* **1963**, *38*, 2042–2043.
- (2) Morel, D. L.; Ghosh, A. K.; Feng, T.; Stogryn, E. L.; Purwin, P. E.; Shaw, R. F.; Fishman, C. High-efficiency Organic Solar Cells. *Appl. Phys. Lett.* **1978**, *32*, 495–497.
- (3) Barlow, S.; Brédas, J. L.; Getmanenko, Y. A.; Giesecking, R. L.; Hales, J. M.; Kim, H.; Marder, S. R.; Perry, J. W.; Risko, C.; Zhang, Y. Polymethine Materials with Solid-State Third-Order Optical Susceptibilities Suitable for All-Optical Signal-Processing Applications. *Mater. Horizons* **2014**, *1*, 577–581.
- (4) Tang, C. W. Two-layer Organic Photovoltaic Cell. *Appl. Phys. Lett.* **1986**, *48*, 183–185.
- (5) Koezuka, H.; Tsumura, A.; Ando, T. Field-Effect Transistor with Polythiophene Thin Film. *Synth. Met.* **1987**, *18*, 699–704.
- (6) Burroughes, J. H.; Bradley, D. D. C.; Brown, A. R.; Marks, R. N.; Mackay, K.; Friend, R. H.; Burns, P. L.; Holmes, A. B. Light-Emitting Diodes Based on Conjugated Polymers. *Nature* **1990**, *347*, 539–541.
- (7) Hiramoto, M.; Fujiwara, H.; Yokoyama, M. Three-layered Organic Solar Cell with a Photoactive Interlayer of Codeposited Pigments. *Appl. Phys. Lett.* **1991**, *58*, 1062–1064.
- (8) Garnier, F.; Hajlaoui, R.; Yassar, A.; Srivastava, P. All-Polymer Field-Effect Transistor Realized by Printing Techniques. *Science* **1994**, *265*, 1684–1686.
- (9) Horowitz, G. Field-Effect Transistors Based on Short Organic Molecules. *J. Mater. Chem.* **1999**, *9*, 2021–2026.

- (10) Hales, J. M.; Matichak, J.; Barlow, S.; Ohira, S.; Yesudas, K.; Brédas, J.-L.; Perry, J. W.; Marder, S. R. Design of Polymethine Dyes with Large Third-Order Optical Nonlinearities and Loss Figures of Merit. *Science* **2010**, *327*, 1485–1488.
- (11) Giesecking, R. L.; Mukhopadhyay, S.; Shiring, S. B.; Risko, C.; Brédas, J.-L. Impact of Bulk Aggregation on the Electronic Structure of Streptocyanines: Implications for the Solid-State Nonlinear Optical Properties and All-Optical Switching Applications. *J. Phys. Chem. C* **2014**, *118*, 23575–23585.
- (12) Gershenson, M. E.; Podzorov, V.; Morpurgo, A. F. Colloquium: Electronic Transport in Single-Crystal Organic Transistors. *Rev. Mod. Phys.* **2006**, *78*, 973–989.
- (13) Coropceanu, V.; Cornil, J.; da Silva Filho, D. A.; Olivier, Y.; Silbey, R.; Brédas, J. L. Charge Transport in Organic Semiconductors. *Chem. Rev.* **2007**, *107*, 926–952.
- (14) Oberhofer, H.; Reuter, K.; Blumberger, J. Charge Transport in Molecular Materials: An Assessment of Computational Methods. *Chem. Rev.* **2017**, *117*, 10319–10357.
- (15) Tessler, N.; Preezant, Y.; Rappaport, N.; Roichman, Y. Charge Transport in Disordered Organic Materials and Its Relevance to Thin-Film Devices: A Tutorial Review. *Advanced Materials*, 2009, *21*, 2741–2761.
- (16) Fratini, S.; Mayou, D.; Ciuchi, S. The Transient Localization Scenario for Charge Transport in Crystalline Organic Materials. *Advanced Functional Materials*, 2016, *26*, 2292–2315.
- (17) Winkler, C.; Mayer, F.; Zojer, E. Analyzing the Electronic Coupling in Molecular Crystals—The Instructive Case of A-Quinacridone. *Adv. Theory Simulations* **2019**, *2*, 1800204.

- (18) Troisi, A.; Orlandi, G. Charge-Transport Regime of Crystalline Organic Semiconductors: Diffusion Limited by Thermal Off-Diagonal Electronic Disorder. *Phys. Rev. Lett.* **2006**, *96*, 086601.
- (19) Ciuchi, S.; Fratini, S.; Mayou, D. Transient Localization in Crystalline Organic Semiconductors. *Phys. Rev. B* **2011**, *83*, 081202.
- (20) Fratini, S.; Ciuchi, S. Bandlike Motion and Mobility Saturation in Organic Molecular Semiconductors. *Phys. Rev. Lett.* **2009**, *103*, 266601.
- (21) Cheng, Y.-C.; Silbey, R. J. A Unified Theory for Charge-Carrier Transport in Organic Crystals. *J. Chem. Phys.* **2008**, *128*, 114713.
- (22) Ortmann, F.; Bechstedt, F.; Hannewald, K. Theory of Charge Transport in Organic Crystals: Beyond Holstein's Small-Polaron Model. *Phys. Rev. B* **2009**, *79*, 235206.
- (23) Fratini, S.; Ciuchi, S.; Mayou, D.; De Laissardière, G. T.; Troisi, A. A Map of High-Mobility Molecular Semiconductors. *Nat. Mater.* **2017**, *16*, 998–1002.
- (24) Kwon, O.; Coropceanu, V.; Gruhn, N. E.; Durivage, J. C.; Laquindanum, J. G.; Katz, H. E.; Cornil, J.; Brédas, J. L. Characterization of the Molecular Parameters Determining Charge Transport in Anthradithiophene. *J. Chem. Phys.* **2004**, *120*, 8186–8194.
- (25) Valeev, E. F.; Coropceanu, V.; Da Silva Filho, D. A.; Salman, S.; Brédas, J. L. Effect of Electronic Polarization on Charge-Transport Parameters in Molecular Organic Semiconductors. *J. Am. Chem. Soc.* **2006**, *128*, 9882–9886.
- (26) Bredas, J. L.; Calbert, J. P.; da Silva Filho, D. A.; Cornil, J. Organic Semiconductors: A Theoretical Characterization of the Basic Parameters Governing Charge Transport. *Proc. Natl. Acad. Sci.* **2002**, *99*, 5804–5809.

- (27) Lemaire, V.; Da Silva Filho, D. A.; Coropceanu, V.; Lehmann, M.; Geerts, Y.; Piris, J.; Debije, M. G.; Van De Craats, A. M.; Senthilkumar, K.; Siebbeles, L. D. A.; *et al.* Charge Transport Properties in Discotic Liquid Crystals: A Quantum-Chemical Insight into Structure-Property Relationships. *J. Am. Chem. Soc.* **2004**, *126*, 3271–3279.
- (28) da Silva Filho, D. A.; Kim, E.-G.; Brédas, J.-L. Transport Properties in the Rubrene Crystal: Electronic Coupling and Vibrational Reorganization Energy. *Adv. Mater.* **2005**, *17*, 1072–1076.
- (29) Kazmaier, P. M.; Hoffmann, R. A Theoretical Study of Crystallochromy. Quantum Interference Effects in the Spectra of Perylene Pigments. *J. Am. Chem. Soc.* **1994**, *116*, 9684–9691.
- (30) Hoffmann, R. Die Begegnung von Chemie Und Physik Im Festkörper. *Angew. Chemie* **2007**, *99*, 871–906.
- (31) Hoffmann, R. A Chemical and Theoretical Way to Look at Bonding on Surfaces. *Rev. Mod. Phys.* **1988**, *60*, 601–628.
- (32) Chung, H.; Diao, Y. Polymorphism as an Emerging Design Strategy for High Performance Organic Electronics. *J. Mater. Chem. C* **2016**, *4*, 3915–3933.
- (33) Diao, Y.; Lenn, K. M.; Lee, W. Y.; Blood-Forsythe, M. A.; Xu, J.; Mao, Y.; Kim, Y.; Reinspach, J. A.; Park, S.; Aspuru-Guzik, A.; *et al.* Understanding Polymorphism in Organic Semiconductor Thin Films through Nanoconfinement. *J. Am. Chem. Soc.* **2014**, *136*, 17046–17057.
- (34) Sutton, C.; Risko, C.; Brédas, J.-L. Noncovalent Intermolecular Interactions in Organic Electronic Materials: Implications for the Molecular Packing vs Electronic Properties of

- Acenes. *Chem. Mater.* **2016**, *28*, 3–16.
- (35) Paulus, E. F.; Leusen, F. J. J.; Schmidt, M. U. Crystal Structures of Quinacridones. *CrystEngComm* **2007**, *9*, 131–143.
- (36) Klues, M.; Witte, G. Crystalline Packing in Pentacene-like Organic Semiconductors. *CrystEngComm* **2018**, *20*, 63–74.
- (37) Campbell, R. B.; Robertson, J. M.; Trotter, J.; IUCr. The Crystal and Molecular Structure of Pentacene. *Acta Crystallogr.* **1961**, *14*, 705–711.
- (38) Park, S. K.; Jackson, T. N.; Anthony, J. E.; Mourey, D. A. High Mobility Solution Processed 6,13-Bis(Triisopropyl-Silylethynyl) Pentacene Organic Thin Film Transistors. *Appl. Phys. Lett.* **2007**, *91*, 063514.
- (39) Reese, C.; Bao, Z. High-Resolution Measurement of the Anisotropy of Charge Transport in Single Crystals. *Adv. Mater.* **2007**, *19*, 4535–4538.
- (40) Anthony, J. E.; Brooks, J. S.; Eaton, D. L.; Parkin, S. R. Functionalized Pentacene: Improved Electronic Properties from Control of Solid-State Order. *J. Am. Chem. Soc.* **2001**, *123*, 9482–9483.
- (41) Haddon, R. C.; Siegrist, T.; Fleming, R. M.; Bridenbaugh, P. M.; Laudise, R. A. Band Structures of Organic Thin Film Transistor Materials. *J. Mater. Chem.* **1995**, *5*, 1719–1724.
- (42) Volkhard May, O. K. *Charge and Energy Transfer Dynamics in Molecular Systems*; 3rd ed.; Wiley-VCH Verlag GmbH & Co. KGaA: Boschstr. 12, 69469 Weinheim, Germany, 2011.

- (43) Davis, W. B.; Svec, W. A.; Ratner, M. A.; Wasielewski, M. R. Molecular-Wire Behaviour in p-Phenylenevinylene Oligomers. *Nature* **1998**, *396*, 60–63.
- (44) Petrovt, E. G.; May, V. A Unified Description of Superexchange and Sequential Donor-Acceptor Electron Transfer Mediated by a Molecular Bridge. *J. Phys. Chem. A* **2001**, *105*, 10176–10186.
- (45) Hopfield, J. J.; Onuchic, J. N.; Beratan, D. N. Electronic Shift Register Memory Based on Molecular Electron-Transfer Reactions. *J. Phys. Chem.* **1989**, *93*, 6350–6357.
- (46) Blum, V.; Gehrke, R.; Hanke, F.; Havu, P.; Havu, V.; Ren, X.; Reuter, K.; Scheffler, M. Ab Initio Molecular Simulations with Numeric Atom-Centered Orbitals. *Comput. Phys. Commun.* **2009**, *180*, 2175–2196.
- (47) Perdew, J. P.; Burke, K.; Ernzerhof, M. Generalized Gradient Approximation Made Simple. *Phys. Rev. Lett.* **1996**, *77*, 3865–3868.
- (48) Perdew, J. P.; Burke, K.; Ernzerhof, M. Erratum: Generalized Gradient Approximation Made Simple (Physical Review Letters (1996) 77 (3865)). *Physical Review Letters*, 1997, *78*, 1396.
- (49) Mayer, F. Electronic Couplings in Molecular Crystals: Development and Benchmarking of Advanced Strategies, Graz University of Technology, 2019.
- (50) Kresse, G.; Hafner, J. Ab Initio Molecular Dynamics for Liquid Metals. *Phys. Rev. B* **1993**, *47*, 558–561.
- (51) Kresse, G.; Hafner, J. Ab Initio Molecular-Dynamics Simulation of the Liquid-Metalamorphous- Semiconductor Transition in Germanium. *Phys. Rev. B* **1994**, *49*, 14251–14269.

- (52) Kresse, G.; Furthmüller, J. Efficiency of Ab-Initio Total Energy Calculations for Metals and Semiconductors Using a Plane-Wave Basis Set. *Comput. Mater. Sci.* **1996**, *6*, 15–50.
- (53) Kresse, G.; Furthmüller, J. Efficient Iterative Schemes for Ab Initio Total-Energy Calculations Using a Plane-Wave Basis Set. *Phys. Rev. B* **1996**, *54*, 11169–11186.
- (54) Tkatchenko, A.; Scheffler, M. Accurate Molecular Van Der Waals Interactions from Ground-State Electron Density and Free-Atom Reference Data. *Phys. Rev. Lett.* **2009**, *102*, 073005.
- (55) Kresse, G.; Joubert, D. From Ultrasoft Pseudopotentials to the Projector Augmented-Wave Method. *Phys. Rev. B* **1999**, *59*, 1758–1775.
- (56) Methfessel, M.; Paxton, A. T. High-Precision Sampling for Brillouin-Zone Integration in Metals. *Phys. Rev. B* **1989**, *40*, 3616–3621.
- (57) Ambrosetti, A.; Reilly, A. M.; Distasio, R. A.; Tkatchenko, A. Long-Range Correlation Energy Calculated from Coupled Atomic Response Functions. *J. Chem. Phys.* **2014**, *140*, 18A508.
- (58) Grimme, S.; Ehrlich, S.; Goerigk, L. Effect of the Damping Function in Dispersion Corrected Density Functional Theory. *J. Comput. Chem.* **2011**, *32*, 1456–1465.
- (59) Heyd, J.; Scuseria, G. E.; Ernzerhof, M. Hybrid Functionals Based on a Screened Coulomb Potential. *J. Chem. Phys.* **2003**, *118*, 8207–8215.
- (60) Heyd, J.; Scuseria, G. E.; Ernzerhof, M. Erratum: Hybrid Functionals Based on a Screened Coulomb Potential (Journal of Chemical Physics (2003) 118 (8207)). *Journal of Chemical Physics*, 2006, *124*, 219906.

- (61) Lüftner, D.; Refaely-Abramson, S.; Pachler, M.; Resel, R.; Ramsey, M. G.; Kronik, L.; Puschnig, P. Experimental and Theoretical Electronic Structure of Quinacridone. *Phys. Rev. B* **2014**, *90*, 075204.
- (62) Thorley, K. J.; Finn, T. W.; Jarolimek, K.; Anthony, J. E.; Risko, C. Theory-Driven Insight into the Crystal Packing of Trialkylsilylethynyl Pentacenes. *Chem. Mater.* **2017**, *29*, 2502–2512.
- (63) Mitoraj, M. P.; Michalak, A.; Ziegler, T. A Combined Charge and Energy Decomposition Scheme for Bond Analysis. *J. Chem. Theory Comput.* **2009**, *5*, 962–975.
- (64) Ryno, S. M.; Risko, C.; Brédas, J. L. Noncovalent Interactions and Impact of Charge Penetration Effects in Linear Oligoacene Dimers and Single Crystals. *Chem. Mater.* **2016**, *28*, 3990–4000.
- (65) Sutton, C.; Marshall, M. S.; Sherrill, C. D.; Risko, C.; Brédas, J. L. Rubrene: The Interplay between Intramolecular and Intermolecular Interactions Determines the Planarization of Its Tetracene Core in the Solid State. *J. Am. Chem. Soc.* **2015**, *137*, 8775–8782.
- (66) Sherrill, C. D. Energy Component Analysis of π Interactions. *Acc. Chem. Res.* **2013**, *46*, 1020–1028.
- (67) Pastorczyk, E.; Corminboeuf, C. Perspective: Found in Translation: Quantum Chemical Tools for Grasping Non-Covalent Interactions. *J. Chem. Phys.* **2017**, *146*, 120901.
- (68) Pecher, L.; Tonner, R. Deriving Bonding Concepts for Molecules, Surfaces, and Solids with Energy Decomposition Analysis for Extended Systems. *Wiley Interdiscip. Rev. Comput. Mol. Sci.* **2018**, e1401.

- (69) Ziegler, T.; Rauk, A. On the Calculation of Bonding Energies by the Hartree Fock Slater Method - I. The Transition State Method. *Theor. Chim. Acta* **1977**, *46*, 1–10.
- (70) Bickelhaupt, F. M.; Baerends, E. J. Kohn-Sham Density Functional Theory: Predicting and Understanding Chemistry. In *Reviews in computational chemistry*; Wiley-VCH Verlag, 2007; Vol. 15, pp. 1–86.
- (71) Zhao, L.; von Hopffgarten, M.; Andrada, D. M.; Frenking, G. Energy Decomposition Analysis. *Wiley Interdiscip. Rev. Comput. Mol. Sci.* **2018**, *8*, e1345.
- (72) Raupach, M.; Tonner, R. A Periodic Energy Decomposition Analysis Method for the Investigation of Chemical Bonding in Extended Systems. *J. Chem. Phys.* **2015**, *142*, 194105.
- (73) Sinnokrot, M. O.; Sherrill, C. D. Substituent Effects in π - π Interactions: Sandwich and t-Shaped Configurations. *J. Am. Chem. Soc.* **2004**, *126*, 7690–7697.
- (74) Wheeler, S. E. Local Nature of Substituent Effects in Stacking Interactions. *J. Am. Chem. Soc.* **2011**, *133*, 10262–10274.
- (75) Stasyuk, O. A.; Sedlak, R.; Guerra, C. F.; Hobza, P. Comparison of the DFT-SAPT and Canonical EDA Schemes for the Energy Decomposition of Various Types of Noncovalent Interactions. *J. Chem. Theory Comput.* **2018**, *14*, 3440–3450.
- (76) te Velde, G.; Bickelhaupt, F. M.; Baerends, E. J.; Fonseca Guerra, C.; van Gisbergen, S. J. A.; Snijders, J. G.; Ziegler, T. Chemistry with ADF. *J. Comput. Chem.* **2001**, *22*, 931–967.
- (77) Fonseca Guerra, C.; Snijders, J. G.; Te Velde, G.; Baerends, E. J. Towards an Order-N DFT Method. *Theor. Chem. Acc.* **1998**, *99*, 391–403.

- (78) Baerends, E. J.; Ziegler, T.; Atkins, A. J.; Autschbach, J.; Bashford, D.; Baseggio, O.; Bérces, A.; Bickelhaupt, F. M.; Bo, C.; Boerritger, P. M.; *et al.* ADF2018, SCM, Theoretical Chemistry, Vrije Universiteit, Amsterdam, The Netherlands, <https://www.scm.com>.
- (79) Van Lenthe, E.; Baerends, E. J. Optimized Slater-Type Basis Sets for the Elements 1-118. *J. Comput. Chem.* **2003**, *24*, 1142–1156.
- (80) Stukowski, A. Visualization and Analysis of Atomistic Simulation Data with OVITO—the Open Visualization Tool. *Model. Simul. Mater. Sci. Eng.* **2010**, *18*, 015012.
- (81) Hanwell, M. D.; Curtis, D. E.; Lonie, D. C.; Vandermeersch, T.; Zurek, E.; Hutchison, G. R. Avogadro: An Advanced Semantic Chemical Editor, Visualization, and Analysis Platform. *J. Cheminform.* **2012**, *4*.
- (82) Gao, H. Z. Theoretical Study on Charge Transport of Quinacridone Polymorphs. *Int. J. Quantum Chem.* **2012**, *112*, 740–746.
- (83) Głowacki, E. D.; Leonat, L.; Irimia-vladu, M.; Schwödiauer, R.; Ullah, M.; Sitter, H.; Bauer, S.; Sariciftci, N. S. Intermolecular Hydrogen-Bonded Organic Semiconductors — Quinacridone versus Pentacene Intermolecular Hydrogen-Bonded Organic Semiconductors — Quinacridone versus Pentacene. *Appl. Phys. Lett.* **2012**, *101*, 0233051–0233055.
- (84) Mei, J.; Diao, Y.; Appleton, A. L.; Fang, L.; Bao, Z. Integrated Materials Design of Organic Semiconductors for Field-Effect Transistors. *Journal of the American Chemical Society*, 2013, *135*, 6724–6746.
- (85) Anthony, J. E. Functionalized Acenes and Heteroacenes for Organic Electronics.

Chemical Reviews, 2006, 106, 5028–5048.

- (86) Okamoto, T.; Nakahara, K.; Saeki, A.; Seki, S.; Oh, J. H.; Akkerman, H. B.; Bao, Z.; Matsuo, Y. Aryl-Perfluoroaryl Substituted Tetracene: Induction of Face-to-Face π - π Stacking and Enhancement of Charge Carrier Properties. *Chem. Mater.* **2011**, 23, 1646–1649.
- (87) McGarry, K. A.; Xie, W.; Sutton, C.; Risko, C.; Wu, Y.; Young, V. G.; Brédas, J.-L. L.; Frisbie, C. D.; Douglas, C. J. Rubrene-Based Single-Crystal Organic Semiconductors: Synthesis, Electronic Structure, and Charge-Transport Properties. *Chem. Mater.* **2013**, 25, 2254–2263.
- (88) Sorli, J. C.; Ai, Q.; Granger, D. B.; Gu, K.; Parkin, S.; Jarolimek, K.; Telesz, N.; Anthony, J. E.; Risko, C.; Loo, Y.-L. L. Impact of Atomistic Substitution on Thin-Film Structure and Charge Transport in a Germanyl-Ethynyl Functionalized Pentacene. *Chem. Mater.* **2019**, acs.chemmater.9b00546.

TOC graphics

